UCLouvain

epl

École polytechnique de Louvain

Numerical simulations of combustion in a porous medium using a one-domain approach

Author: **Eric Bisa**
Supervisors: **Miltiadis Papalexandris, Victoria Hamtiaux**
Readers: **Véronique Dias, Francesco Contino**
Academic year 2019–2020
Master [120] in Mechanical Engineering

Acknowledgements

Foremost, I would like to express my sincere gratitude to my supervisors Miltiadis Papalexandris and Victoria Hamtiaux for their support, guidance, motivation, patience throughout the year.

I would also like to thanks my parents: Lucie Niyonzima and Bisanukuri Pierre for their moral support and enthousiasm during the writting of this master thesis.

Computational resources have been provided by the supercomputing facilities of the Université catholique de Louvain (CISM/UCL) and the Consortium des Équipements de Calcul Intensif en Fédération Wallonie Bruxelles (CÉCI) funded by the Fond de la Recherche Scientifique de Belgique (F.R.S.-FNRS) under convention 2.5020.11 and by the Walloon Region

Contents

List of Figures

Chapter 1

Introduction

A material can be considered as a porous medium if it contains relatively small spaces free of solids, so-called pores or voids, embedded in the solid matrix [8]. Many natural substances (e.g. rocks and soil, bones, wood, etc.) and man-made materials (e.g. cement, ceramics, etc.) can be considered as porous media.

This work only addresses media having pores that form an interconnected phase within the material. This allows the transport of matter across the porous medium. In this work, we consider fluids flow in domains partly occupied by a region that contains a fluid alone and partly by a porous medium which is saturated by the same fluid.

This master thesis is based on the Ph.D. Thesis “Modelling and numerical simulation of transient flows in superposed porous and pure-fluid layers" by Panagiotis Dimitrios Antoniadis.

1.1 State of the art

1.1.1 Combustion in porous medium

Most of the studies of combustion in porous mediums have been based on the two-domain approach. According to it, separate governing equations are prescribed on the porous medium and the pure-fluid model like in [14]. However, in this work, we use a single-domain approach. The study of combustion in porous medium

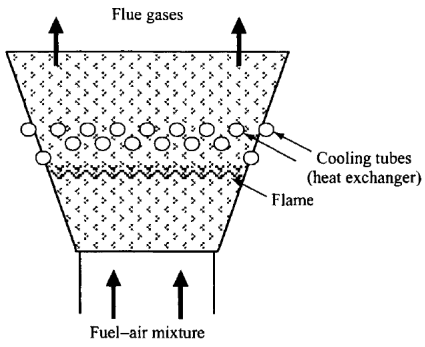

Figure 1.1: Boiler using combustion in porous media [7]

has various practical technological applications. In surface burners and advanced boilers, the combustion can be improved and the size of the boilers can be reduced by using the concept of combustion in porous media (see figure 1.1). Such a boiler has the ability of a wide power modulation, it can be modulated without scarifying efficiency and emits less pollution [7].

In internal combustion engines, it is possible to generate super-adiabatic combustion in a porous medium. In [12], a numerical simulation of the performances of a reciprocating heat engine with super-adiabatic combustion in porous media was performed. The results showed that the maximum temperature and the efficiency of the engine were higher. Similar results were obtained from experiments of natural gas combustion in porous burners in [15] . Furthermore, super-adiabatic burners can also be used in plasma application and direct thermal-electric conversion, etc.

In propulsion gas turbine, the combustion in porous media allows a leaner, hotter burn with low emission and free from combustion-induced noise. Furthermore, no cooling would be necessary for the combustor [9].

1.1.2 Combustion in canopies

The combustion and fire spread, when occurring in canopies, are difficult to simulate due to the complexity and the non-linearity of these systems. Multiples models have been developed to simulate the behavi our of a forest canopy fire.

Some rely on Cellular Automaton (CA) like in [13]. The model was applied to the March 2014 Dumai forest fire, it was satisfactorily accurate in predicting its evolution. CA can also be combined with Extreme Learning Machine (ELM) like

in [24]. By integrating the ELM in the classical forest fire CA framework, a new cellular automaton modelling approach is conceived. Furthermore, comparing the model prediction against actual fire observations shows that the performances are in most cases better than the traditional CA framework's. Other models rely on two-way coupling algorithm like in [2]. Theses type of models take into account the interaction (two-way coupling) between fire and wind instead of assuming that the wind field is undisturbed by thermal effects. This allows the model to take into account buoyancy effects.

Even though a lot of models are in 2-D, 3-D models are also sometimes used like in [17]. In that work, results are obtained by solving the governing equations of fluid dynamics, combustion, heat transfer and thermal degradation of the vegetative fuel.

Some works focus on smoke modelling like in [1]. In that paper, simulations and experiments of hypothetical prescribed burns are used to understand the new and improved capability required for the next-generation smoke research and forecasting systems.

1.2 Scope of the work

Combustion reactions inside and around a porous medium involve complex chemical and thermodynamic phenomenon. As presented in the previous section, there have been multiple models developed and experiments conducted to obtain realistic models. The method implemented in this work uses a single domain approach. This means that, instead of having a set of equations for the porous medium and a set of equations for the fluid, we use a single set of governing equations that are simultaneously valid in both the porous and the pure-fluid domains. In this approach, the volume fraction of the fluid phase (i.e. the porosity) is introduced as a field variable.

The Ph.D. thesis of Panagiotis [3] studied the 2D flow and heat transfer of air inside and around a porous medium. In that thesis, a simple combustion model was proposed. In this work, the combustion model is improved by taking into account the effects the combustion products have on the flow. Indeed, combustion reactions generate chemical compounds usually observable in the form of smoke emanating from the flame. The presence of theses compounds impacts the flow of fluids around the reaction zone.

In chapter 2, the mathematical model developed in [3] and its corresponding numerical application are briefly described, in chapter 3 the combustion model used in this work is explained. In chapter 4, the combustion model is applied to a classical chemical reaction: the complete combustion of carbon. The numerical simulations of combustion presented in [3] are performed using this time the new combustion model. Finally, in chapter 5 a fire occurring on a canopy is simulated.

Chapter 2

Porous medium modelisation

2.1 Introduction

In this chapter, we present the thermo-mechanical model of the flows of interest, based on the one-domain approach. To this extent, we adopt a mixture-theoretic formalism under which the fluid and the porous medium are treated as two separate and identifiable continua that occupy the same space and that are in thermodynamic non-equilibrium with each other.

The modelling used in this work follows the mixture-theoretic formalism of Papalexandris [21], which is a generalisation of the classical theory of irreversible processes to immiscible mixtures whose constituents are in thermal non-equilibrium.

The limiting case of incompressible flows is derived via the "*Low Mach Number Approximation*" instead of assuming that the density or the pressure of the fluid are constants. Under this approximation, the thermodynamic pressure appears only in the energy equation of the fluid phase, and not in the momentum equation. This greatly simplifies the equations and the constitutive expressions of the interphasial mass exchange. The numerical algorithm implemented to solve the thermo-mechanical equations uses a two-step advancement method and the spatial discretisation is performed on a collocated grid.

The chapters are organized as follows, in section 2.2 the thermo-mechanical model is shortly explained and in section 2.3 the numerical algorithm is briefly presented.

2.2 Mathematical model

The derivation of the mathematical model is detailed in the work of Antoniadis [3]. We will only focus on the important steps.

Thermo-mechanical model

Let $\Omega \subset \mathbb{R}^3$ be an open and bounded domain that contains both saturated porous and pure-fluid regions. The porosity distribution $\phi(\boldsymbol{x}, t)$ is introduced as a concentration parameter that measures the density of volume occupied by the fluid. According to [5], $\phi(\boldsymbol{x}, t)$ is a probability density function defined in Ω and take values in the interval [0,1].
Let $\Omega_p \subset \Omega$ be the subdomain that is covered by the porous material, $\Omega_p = \{\boldsymbol{x} \in \Omega : \phi(\boldsymbol{x}, t) < 1\}$. Similarly, let $\Omega_f \subset \Omega$ be the subdomain that is covered by pure fluid, $\Omega_f = \{\boldsymbol{x} \in \Omega : \phi(\boldsymbol{x}, t) = 1\}$. Also, let S_Ω denote the boundary between Ω_p and Ω_f. Since Ω_p is an open subset of Ω, along S_Ω we have that $\phi(\boldsymbol{x} \in S_\Omega, t) = 1$.
The assumptions of our model are based on the following :

1. Each phase is modelled as a continuum thermodynamic system.
2. The two thermodynamic continua are immiscible but occupy the same space. In particular, they fill completely the space that they occupy (saturation condition).
3. The two thermodynamic continua are open to each other and at non-equilibrium.
4. The mass, momentum and energy exchanges between the two continua are pure, i.e. their sum must vanish.
5. The skeleton (or matrix) of the porous material is assumed to be a rigid solid of zero velocity and constant mass density. Also, the fluid is assumed to be simple and isotropic.
6. The postulate of phase separation holds. In other words, irreversible phenomena associated with only one phase do not depend on the variables of the other phase.

The two thermodynamic systems can interact with each other, these interactions are in the form of mass, momentum, and energy exchanges, and are denoted by

$\mathcal{M}$, $\boldsymbol{f}$, and $\boldsymbol{\varepsilon}$, respectively. In this work, we follow the framework described by Papalexandris in [18] to immiscible mixtures whose constituents are in thermal non-equilibrium. We can then define ρ, $\boldsymbol{u} = (u, v)$, p, e_t that respectively denote the density, velocity vector, pressure and total energy of the fluid. All variables relative to the fluid phase only, are defined in the entire domain. In view of the constitutive assumptions (1)-(4), and after some algebraic operations, the mass, momentum and energy balance laws for the fluid phase are :

$$\frac{\mathrm{d}(\phi\rho)}{\mathrm{d}t} + \phi\rho\nabla\cdot\boldsymbol{u} = \mathcal{M} \tag{2.1}$$

$$\phi\rho\frac{\mathrm{d}\boldsymbol{u}}{\mathrm{d}t} + \nabla(\phi p) = \nabla\cdot(\phi\boldsymbol{P}^v_d) - \nabla(\phi p^v) + \boldsymbol{f} - \mathcal{M}\boldsymbol{u} + \phi\rho\boldsymbol{g} \tag{2.2}$$

$$\phi\rho\frac{\mathrm{d}e}{\mathrm{d}t} + \phi p\nabla\cdot\boldsymbol{u} = \phi\boldsymbol{P}^v_d : \boldsymbol{V}^v_d - \phi p^v\nabla\cdot\boldsymbol{u} - \nabla\cdot(\phi\boldsymbol{q}) + \boldsymbol{\varepsilon} - \boldsymbol{f}\cdot\boldsymbol{u} - \mathcal{M}(e - \frac{1}{2}\boldsymbol{u}\boldsymbol{u}) \tag{2.3}$$

where $\boldsymbol{V^v_d}$ stands for the deviatoric part of the deformation tensor, d/dt() stands for the material derivative with respect to the fluid velocity, and the total energy e_t is the sum of the fluid's internal and kinetic energies:

$$e_t = e + \frac{1}{2}\boldsymbol{u}\cdot\boldsymbol{u} \tag{2.4}$$

In the above equations, q is the conductive heat flux for the fluid phase, g is the vector of gravitational acceleration and $\boldsymbol{P}^v$ Pv is for the viscous stress tensor of the fluid. By virtue of the isotropy of the fluid and the conservation of angular momentum, this tensor is symmetric. It is then decomposed according to:

$$\boldsymbol{P}^v = -p^v\boldsymbol{I} + \boldsymbol{P}^v_d \qquad p^v = -\frac{1}{3}tr\,(\boldsymbol{P}^v) \tag{2.5}$$

where p^v is the bulk viscous pressure and $\boldsymbol{P}^v_d$ is the (deviatoric) viscous shear stress tensor.

Similarly, let ρ_s, p_s, e_s denote the density, pressure (trace of the stress tensor) and internal energy of the solid matrix, respectively. These variables, and all variables to the solid matrix only, are defined in the porous region Ω_p. By virtue

of the assumptions (1)-(5), and knowing that the density of the solid phase is constant, the balance laws for the solid matrix read:

$$\frac{\partial \phi}{\partial t} = \frac{1}{\rho_s}\mathcal{M} \tag{2.6}$$

$$\nabla((1-\phi)p_s) + \nabla \cdot ((1-\phi)\boldsymbol{\tau}_s) = -\boldsymbol{f} + (1-\phi)\rho_s \boldsymbol{g} \tag{2.7}$$

$$(1-\phi)\rho_s \frac{\partial e_s}{\partial t} = -\nabla \cdot ((1-\phi)\boldsymbol{q}_s) - \boldsymbol{\varepsilon} + \mathcal{M} e_s \tag{2.8}$$

where τ_s and $\boldsymbol{q}_s$ stands for the deviatoric part of the stress tensor and the conductive heat flux of the solid matrix, respectively.

In the appendix A, the next steps leading to a complete mathematical model are detailed.

Low Mach Number Assumption

When the fluid velocity is small with respect to the speed of sound, the compressibility effects can be neglected. It is possible to use the square of the Mach number as a perturbation parameter and perturb the governing system of equations. This procedure gives us a perturbed system that is simpler known as *low Mach number approximation*.

The derivation procedure is standard and is detailed in [4]. The basic steps of the derivation can be found in [3].

During the derivation, we considered a set of reference variables. The perturbation parameter ϵ is linked to the speed of sound by the relation $\epsilon = \gamma(u_{ref}/c)^2$. All variables are expanded in perturbation series of powers of ϵ, for example

$$p = p^0 + \epsilon\, p^1 + O(\epsilon^2) \qquad \boldsymbol{u} = \boldsymbol{u}^0 + \epsilon\, \boldsymbol{u}^1 + O(\epsilon^2) \qquad \text{etc.} \tag{2.9}$$

After the procedure, the balance laws of the fluid phase (2.1)-(2.3) becomes

$$\frac{\mathrm{d}(\phi^0\rho^0)}{\mathrm{d}t} + \phi^0\rho^0\nabla\cdot\boldsymbol{u}^0 = \kappa\mathcal{A}^0 \tag{2.10}$$

$$\begin{aligned}\phi^0\rho^0\frac{\mathrm{d}\boldsymbol{u}^0}{\mathrm{d}t} + \phi^0\nabla p^1 =& \frac{1}{Re}\nabla\cdot(\phi^0\mu\boldsymbol{V}_d^{v0}) + \frac{1}{Re}\nabla(\phi^0\zeta\nabla\cdot\boldsymbol{u}^0) \\ & - \underset{\sim}{\boldsymbol{\beta}}\boldsymbol{u}^0 - Ri\phi^0\rho^0\hat{\boldsymbol{y}} - \kappa\mathcal{A}^0\boldsymbol{u}^0\end{aligned} \tag{2.11}$$

$$\phi^0\rho^0 c_p\frac{\mathrm{d}T^0}{\mathrm{d}t} - \phi^0\frac{\gamma-1}{\gamma}\frac{\partial p^0}{\partial t} = \frac{1}{RePr}\nabla\cdot(\phi^0 k\nabla T^0) + h(T_s^0 - T^0) - \kappa\mathcal{A}^0\left(e + \frac{\gamma-1}{\gamma}\left(\frac{p^0}{\rho^0} - \frac{p^0}{\rho_s^0}\right)\right) \tag{2.12}$$

where Re and Pr are the Reynolds and Prandtl numbers with respect to the reference variables. Also, $Ri = |\boldsymbol{g}|l_{ref}/u_{ref}^2$ stands for the Richardson number and $\hat{\boldsymbol{y}}$ is the unit vector in the direction opposite to the gravitational force. Furthermore, $\mathcal{A}^0$ is the affinity of the interphasial mass exchange, μ and ζ are respectively the fluid shear and bulk viscosities, k and $\underset{\sim}{\boldsymbol{k}}_s$ are respectively the fluid and solid conductivities.

Likewise, the balance laws for the solid phase (2.6)-(2.8) becomes

$$\frac{\partial\phi^0}{\partial t} = \frac{1}{\rho_s^0}\kappa\mathcal{A}^0 \tag{2.13}$$

$$(1-\phi^0)\rho_s^0 c_s\frac{\partial T_s^0}{\partial t} = \frac{1}{RePr}\nabla\cdot\left((1-\phi^0)\underset{\sim}{\boldsymbol{k}}_s\nabla T_s^0\right) \tag{2.14}$$

The solid matrix is assumed to be a rigid body. Its equation of balance of forces , after the application of the low Mach number approximation, becomes inconsequential for the flows of interest and, therefore is omitted. An important advantage resulting from the low-Mach number approximation is that the thermodynamic pressure appears only in the fluid's energy equation and not in the momentum equation. This greatly simplifies the numerical algorithm used for the treatment of the governing equations. All of the work presented from this point onward, is based on the governing equations (2.10) to (2.14).

$\hat{l}_{ref}$ $[m]$	$7.23 \cdot 10^{-3}$
$\hat{u}_{ref}$ $[m/s]$	0.755
$\hat{T}_{ref}$ $[K]$	300
$\hat{\rho}_{ref}$ $[kg/m^3]$	1.117
$\hat{\mathcal{R}}_{ref}$ $[cal/(mol\ K)]$	1.987

Table 2.1: Reference values

Modelisation of the porous medium

The drag parametrization with respect to the porosity of the highly porous medium microstructure is modelled after a dilute conglomerate of identical and uniform cylinders. The cylinders are assumed to be parallel to each other and aligned vertically (y-direction) to the bottom boundary of the domain.

2.3 Numerical Algorithm

The complete explanation of the time and spacial discretizations are detailed in the thesis of Panagiotis [3]. The algorithm was implemented in C++. From now on, the dimensional variables will have a $\wedge$ on top of them and the non-dimensionalized variables will be written without it. In the algorithm of Panagiotis, all variables are non-dimensionalized with respect to the reference variables. The values of the reference variable are available on table 2.1.

2.3.1 Time discretization

For improved accuracy in time and stability, in this work, we use a two-step advancement algorithm. First, a preliminary evaluation of the variables performed at the "predictor" step. This step gives us a first rough approximation of the integral value. Secondly, using the values obtained in the predictor step, the variables are updated in the "corrector" step. The order of computation at each step of the main variable can be seen on figure 2.1.

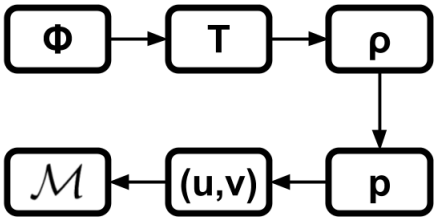

Figure 2.1: Order of computation at each step

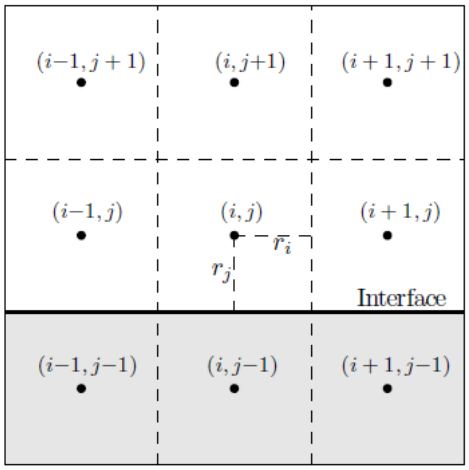

Figure 2.2: Representation of grid cells at the vicinity of the porous medium/pure fluid interface.The shaded area indicates the part of the domain that is occupied by the porous medium.[3]

2.3.2 Spacial discretization

The spatial discretization of the governing equations is performed on a collocated grid system. On a collocated grid, all flow variables are stored at the same location, which is in our case the centre of the grid. The grid cells are uniquely identified in indices (i, j), corresponding to the cell's order of appearance along the x, y axis respectively. The dimensions of each cell are $(2r_i, 2r_j)$, r_i and r_j are the distances of the cell interfaces in the 2 directions from the centre of the cell (see figure 2.2). For the convective terms, the speed is interpolated on the interfaces of the cells using finite-difference operators.

Chapter 3

Combustion modelisation

3.1 Introduction

Combustion is the highly exothermic physico-chemical process of oxidation of a fuel [19]. In this work, we only focus on heterogeneous combustion. The combustions are modeled as a one-step chemical reaction that convert solid materials into gaseous products.

The chapters are organised as follows, in section 3.2 the initial combustion model is presented, in section 3.3, the modelisation of the change in the gas constitution due to the combustion is presented, in section 3.4, a model simulating the combustion of carbon is explained and finally, in section 3.5 a similar model simulating a canopy combustion is described.

3.2 Initial model

In the model of the thesis of Panagiotis, the expressions used for the transport parameters of the porous orthotropic medium are inspired by those of an ensemble of vertical cylindrical elements that are identical to each other. The cylinders are assumed to be uniformly distributed and to sparsely populate the porous material.

In this model, the fluid phase is assumed to be composed of a single chemical species. The 2 phases reach with each other at the interface of the micro-structural

elements via the following single-step combustion:

$$\text{Solid} \longrightarrow \text{Gas} + \text{Q} \tag{3.1}$$

In this equation Q is the heat of reaction, which is absorbed by the fluid phase. The interphasial mass exchange rate $\mathcal{M}$, introduced in the equation (2.6), is calculated using a single-step Arrhenius-type expression adapted so as to express the rate of mass exchange at the surface of the cylindrical elements of the solid micro-structure. After non-dimensionalization, we have

$$\mathcal{M} = K_R \frac{4(1-\phi)}{d_p} e^{-\frac{E}{T}} \tag{3.2}$$

where K_R is the pre-exponential factor non-dimensionalized with $\hat{\rho}_{ref}\hat{u}_{ref}$. E is the activation energy non-dimensionalized with $\hat{\mathcal{R}}\hat{T}_{ref}$, with $\hat{\mathcal{R}}$ being the universal gas constant, T is the fluid temperature non-dimensionalized with $\hat{T}_{ref}$ and d_p is the diameter of a single element of the solid matrix. The combustion reaction results in the consumption of the solid matrix. Therefore, the volume of the burning micro-structural elements is reduced.

3.3 Hot gas constituents

The new models of this work compute the position and concentration of the different species of the medium (i.e. oxygen and carbon dioxide, etc.) and also the resulting change of density.

To compute the mass concentrations, we use the balance law of the species from [19]. This gives us the following equation for the i-th constituent in a mixture of r constituents

$$\rho \frac{dY_i}{dt} = \nabla \cdot (\rho \mathcal{D}_i \nabla Y_i) + \dot{\omega}_i M_i \qquad i = 1, ..., r \tag{3.3}$$

In this equation, ρ is the fluid density, Y_i, $\mathcal{D}_i$, $\dot{\omega}_i$ and M_i are respectively the mass fraction, the mass diffusivity, the molar rate of consumption and the molar mass of the species i. For the numerical implementation of the code, the quantities of the equation are dimensionalized and Y_i is computed using the values of the other variables. This gives us :

$$\frac{\partial Y_i}{\partial t} = -\left(\hat{u}\frac{\partial Y_i}{\partial x} + \hat{v}\frac{\partial Y_i}{\partial y}\right) + \frac{1}{\hat{\rho}}\left[\hat{\rho}\hat{\mathcal{D}}_i\left(\frac{\partial Y_i}{\partial x} + \frac{\partial Y_i}{\partial y}\right) + \hat{\dot{\omega}}_i\hat{M}_i\right] \qquad i = 1, ..., r \quad (3.4)$$

The values of u, v and ρ are computed by the original code and the value of the mass diffusivity $\mathcal{D}_i$ can be found in the literature.

To compute the change in density resulting from the variation of the mass concentration, we start from the ideal gas law

$$\hat{p} = \hat{\rho}\hat{R}\hat{T} \quad (3.5)$$

where $\hat{R} = \frac{\hat{\mathcal{R}}}{\hat{M}_{gas}}$ is the ideal gas law constant of the fluid. At the beginning of the simulation, the fluid occupying the entire domain is air. The non-denationalisation of this law is done using the reference values and we obtain $\hat{R}_{ref} = \hat{R}_{air}$. The non-denationalised formula of the density is then

$$\rho = \frac{p}{RT} \quad (3.6)$$

In the model of Panagiotis (section 3.2) , since the constitution of the fluid never changed, we always had $R = 1$. In this work, the value of R changes after the combustion. We can rewrite the value of R as

$$R = \frac{\hat{R}}{\hat{R}_{ref}} = \frac{\hat{\mathcal{R}}/\hat{M}_{mix}}{\hat{\mathcal{R}}/\hat{M}_{air}} = \frac{\hat{M}_{air}}{\hat{M}_{mix}} \quad (3.7)$$

where $\hat{M}_{mix}$ is the molar mass of the mixture of air and combustion products. We know from the course *Combustion and fuels* [19] that

$$\hat{M}_{mix} = \frac{1}{\sum_i \frac{Y_i}{\hat{M}_i}} \quad (3.8)$$

After the implementation of theses changes the order of computation of the main variables is modified. The new order can be seen on figure 3.1.

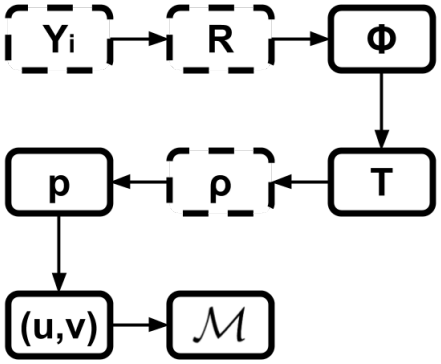

Figure 3.1: Order of computation of the main variables. The added/changed variabled are framed with dashed lines.

3.4 Carbon combustion model

In this model, the parametrization of the transport coefficient, the value of the reference quantities and the expression of the diameter of the cylindrical elements of the solid matrix d_p is the same as in the initial model. However, the combustion equation is different. The solid matrix consumes oxygen during its combustion. The chemical reaction of this model is then a complete combustion of carbon in the air

$$\mathrm{C_{(s)}} + \mathrm{O_{2(g)}} \longrightarrow \mathrm{CO_{2(g)}} + \mathrm{Q} \tag{3.9}$$

We suppose air is only composed of oxygen and nitrogen in the following concentrations

$$[\mathrm{N_2}] = 79\% \qquad [\mathrm{O_2}] = 21\%$$

We neglected the nitrogen in the air since it does not intervene in the reaction. We know that the mass fraction of O_2 and CO_2 respects the equation (3.3). We also know that $\mathcal{M} = \hat{\omega}_C \hat{M}_C$ and we know the stoichiometry of the chemical reaction (3.9), we can then write

$$\hat{\omega}_{CO_2} \hat{M}_{CO_2} = -\hat{\omega}_{0_2} \hat{M}_{O_2} = -\mathcal{M} \frac{\hat{M}_{O_2}}{\hat{M}_C} \tag{3.10}$$

Using all theses information, we can compute the mass fraction of the gaseous species in the fluid and therefore follow their movement in the domain. The source term $\hat{\omega}_i \hat{M}_i$ in the equation (3.3) is therefore proportional to the interphasial mass

exchange $\mathcal{M}$ which is never equal to zero (see equation (3.2)). To avoid taking into account false burning values at low temperature, in the implementation of this model, the source term is neglected when $T < 3$.

Furthermore, as shown on figure 3.1, once the mass fractions are known, we can compute the value of R based on the molar mass of the mixture. In this case, we have

$$\hat{M}_{mix} = \frac{1}{\frac{Y_{0_2}}{\hat{M}_{0_2}} + \frac{Y_{C0_2}}{\hat{M}_{C0_2}} + \frac{Y_{N_2}}{\hat{M}_{N_2}}} \tag{3.11}$$

3.5 Canopy fire

As in the previous model, the parametrization of the transport coefficient, the value of the reference quantities and the expression of the diameter of the cylindrical elements of the solid matrix d_p is the same as in the initial model. However, the combustion equation models a fire in a canopy. In this model, the porous medium represents the capony of a forest and the canopy fire is modelled as a combustion reaction of a compound of type $CH_xO_yN_z$. We suppose that our forest canopy behaves like the one in a maple tree forest, according to [20], the forest can be approximated by the following compound : $CH_{1.46}O_{0.6}N_{0.0035}$. Furthermode, we suppose the combustion to be incomplete for the carbon but complete for the nitrogen in the compound. This gives us the following chemical reaction :

$$\mathrm{CH_{1.46}O_{0.0035}} + \mathrm{mO_2} \longrightarrow (1-\mathrm{k})\mathrm{CO_2} + \mathrm{kCO} + 0.73\mathrm{H_2O} + 0.0035\mathrm{NO_2} + \mathrm{Q} \tag{3.12}$$

where k is the coefficient of unburned carbon and m is the stochiometric coefficient of oxygen. According to [22], we can approximate the value of the coefficient of unburned carbon to k=0.11. The reaction of combustion is then

$$\mathrm{CH_{1.46}O_{0.0035}} + 0.9785\mathrm{O_2} \longrightarrow 0.89\mathrm{CO_2} + 0.11\mathrm{CO} + 0.73\mathrm{H_2O} + 0.0035\mathrm{NO_2} + \mathrm{Q} \tag{3.13}$$

In this model, the NO_2 is used to represent all the NO_x produced by the combustion. This model allows us to follow the propagation and the concentration of the different products of a forest fire. Furthermore, as we did for the carbon combustion model, once the mass fractions are known, we can compute the value of R and therefore ρ based on the molar mass of the mixture. In this case, we have

$$\hat{M}_{mix} = \frac{1}{\frac{Y_{0_2}}{\hat{M}_{0_2}} + \frac{Y_{C0_2}}{\hat{M}_{C0_2}} + \frac{Y_{C0}}{\hat{M}_{C0}} + \frac{Y_{H_2O}}{\hat{M}_{H_2O}} + \frac{Y_{NO_2}}{\hat{M}_{NO_2}}} \tag{3.14}$$

Chapter 4

Carbon combustion

4.1 Introduction

The combustion of carbon is one of the most known chemical reaction. The heat released by this process is the main energy source of coal-fired power plant. Being the main fuel of the industrial revolution, there has been a lot of different modelization of this process.

In practice, carbon combustion is a complex phenomenon involving different physico-chemical processes (incomplete combustion, pyrolysis, etc.). In this chapter, we will study a simplified model of combustion: subsonic combustions producing laminar flames. Furthermore, we will suppose that the combustion is a single-step reaction in which the nitrogen in the air is completely non-reactive, even at high temperatures.

In the following chapters, we will compare the results obtained in this work to the ones obtained in the Ph.D thesis of Panagiotis [3]. His simulations will be referred to as the "original" simulations or the "initial" simulations.

This chapter is organised as follows, in section 4.2 the set-up of the simulation is explained. In section 4.3 the carbon combustion model is applied to a spark ignition combustion and finally in section 4.4 this same model is applied to a combustion induced by an inflow of hot oxidizer.

4.2 Simulation set-up

The porous fuel is assumed to be a square block and the dimension of its sides is l. The initial porosity of the porous medium is $\phi^0 = 0.9$ and the characteristic length of its microstructure is $d_p^0 = 0.0032l$. Moreover, the dimensions of the domain in the streamwise and cross-stream directions are set to $L_x = 12l$ and $L_y = 4l$ respectively. Along the streamwise direction, the porous medium is placed in the channel from $x = 5l$ to $x = 6l$. At the start of the simulation, the domain is isothermal and the 2 phases are in thermal equilibrium. The non-dimensional parameters of the chemical reaction are $K_R = 250$, $E = 18$ and $Q = +3$. Based of the reference parameters value (see table 2.1), the Reynolds number is set to $Re = 350$, the Prandtl number is $Pr = 0.71$ and the Richardson number is $Ri = 0.125$. In this work, the initiation of the ignition process is done using 2 techniques: "hot inflow ignition" and "spark ignition".

In the case of hot inflow ignition, we consider that the porous medium is cold and placed at the half-width of a channel. The chemical reaction is initiated through the exposure of the porous medium to a stream of hot oxidizer. The temperature of the fuel increases progressively because of the hot oxidizer, and once it is sufficiently high, the reaction is started.

The porous block is placed at the half-distance between two parallel walls, i.e. it extends from $y = 1.5l$ to $y = 2.5l$. The oxidizer inflow is modelled as a hot fluid inflow entering the domain. At the inflow boundary, the fluid temperature T_{in} evolves according to the following expression:

$$T_{in}(t) = \begin{cases} 1 + \frac{1.5}{4}t & t < 4 \\ 2.5 & t \geq 4 \end{cases} \tag{4.1}$$

where t is non-dimensionalized with $\frac{\hat{l}_{ref}}{\hat{u}_{ref}}$. At the outflow, we use a convective boundary condition for the temperature, while the top and bottom walls are assumed to be adiabatic.

In the case of spark ignition, the porous fuel is placed next to the lower wall of a channel. The temperature of the porous fuel is raised locally using a heat source for a short time-window until the reaction becomes self-sustainable. For the ignition of the reactants, an external heat source is applied over a non-dimensional area 0.08x0.08 unit lengths at the upper upstream corner of the porous strip, until $t = 3$.

4.3 Spark ignition

4.3.1 Original resuls

Figure 4.1 shows the temperature and the porosity of the porous medium at 4 moments of the original simulation found in the thesis of Panagiotis [3]. We can see that at the beginning of the simulation, the heat flow source increases the fluid temperature progressively until the reaction rate is significant enough to start at $t = 1.5$ when the temperature raises to $T = 3.5$. As we can see on figure 4.1b1 the diffusion of the heat of the reaction increases the temperature of and expands the fluid around the corner of the porous medium. Inside the material, the hot fluid progress symmetrically around the corner.

Furthermore, on figure 4.1b2, we can see that at $t = 2$, the consumption of the porous medium starts. This consumption of the material spreads radially inside the centre of the porous medium. At $t = 2.85$, the hot fluid occupies the whole porous medium and some fluid escapes from it through the downstream interface at $x = 6$. At this stage, the flows stop spreading radially from the heat source. It interacts with the oncoming cold fluid and is stopped in its course at the centerline of the channel. This results in the formation of two principals plumes of hot fluid.

In the first plume, buoyancy effects dominate and cause the fluid to rise to higher in the domain. This plume also reacts with the established cold-fluid inflow that causes it to drift downstream, forming a swirl in the centerline of the channel. As the flow evolves, the size of this swirl increases and reaches a point where it interacts with the boundary layer of the top wall of the channel. This swirl can be seen on figure 4.1d1 at from $x = 8$ to $x = 10$. The second plume travels upstream in front of the reacting zone while remaining close to the bottom wall. This leads to the formation of a positive vorticity roller. At $t = 4.1$, this plume has moved close to the upstream boundary of the domain.

The burning of the porous medium is not limited to the top upstream corner. As we can see of figure 4.1d2, the consumption of the porous medium is more important in the areas close to the center than the ones close to the interfaces. This phenomenon is due to the fact that the fluid velocity is higher close to the interface areas, so heat is convected faster is these areas. At the end of the simulation, the solid matrix is reduced by 67% near the heat source, by 50% at the center of the porous bock and by 7% at the downstream interface of the porous medium.

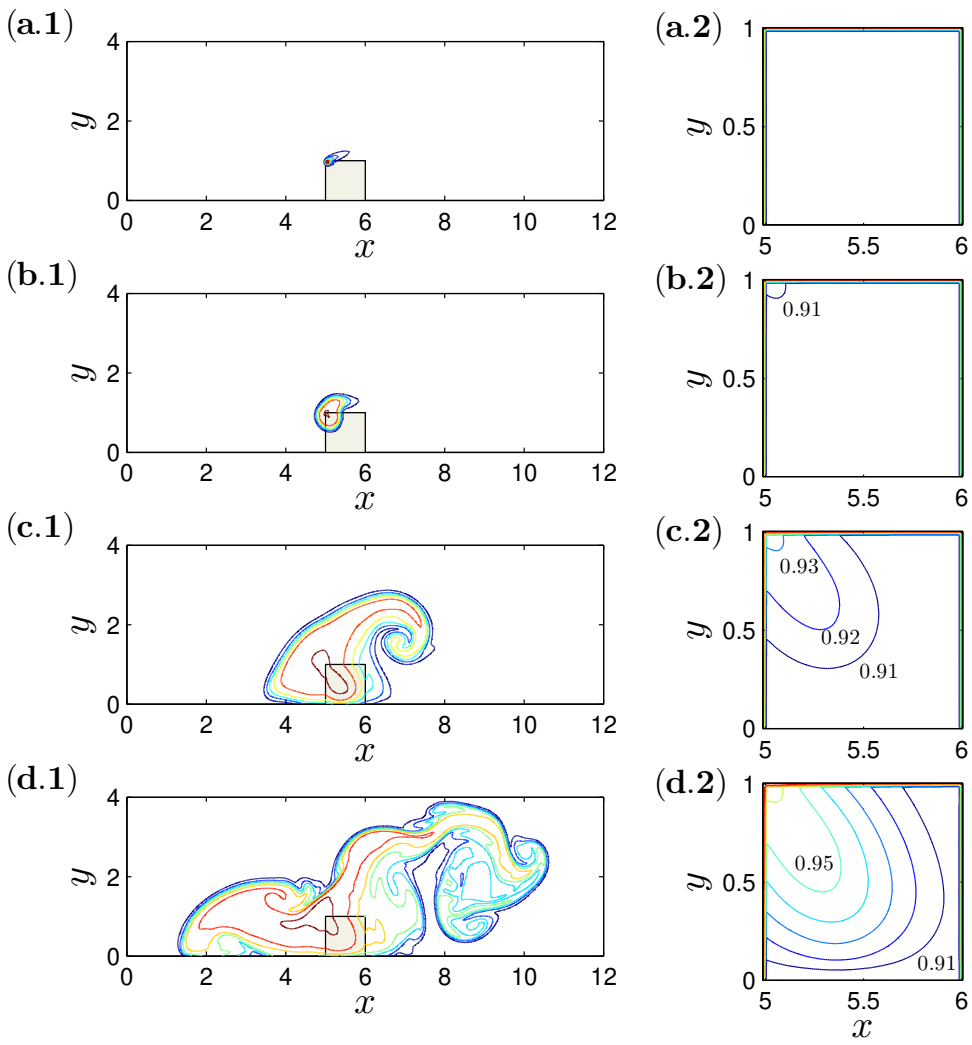

Figure 4.1: Original simulation of the burning porous block placed next to the bottom wall of a pure-fluid channel. Fluid-temperature field (left) and fluid volume fraction (right) at four instances during the evolution of the flow. (a) t = 1.45; (b) t = 2.0; (c) t = 2.85; (d) t = 3.86 [3]

4.3.2 Carbon combustion model results

We are now going to analyse the results of the same experiments using the carbon combustion model presented in section 3.4. Figure 4.2 shows the temperature and

the porosity of the porous medium at 4 moments of the carbon combustion model simulation. We can see on figures 4.2a1 and 4.2b1 that before the start of the combustion reaction, the behaviour of this simulation is exactly the same as the original one. When the temperature raises to $T = 3.5$, the reaction starts and the air around the top upstream corner starts to absorb the heat of the reaction and expand.

We can see on figure 4.2c1 that the first plume of hot air raises slower than in the original simulation. Furthermore, the top part of this swirl travels less far. The upward travel of the second plume is also slower. Overall, the expansion rate of the fluid heated by the reaction is lower than in the original simulation. On the figures 4.2b1 and 4.2c1, we can see that the increase of ϕ also travels from the corner of the porous block to its center. However, the material's combustion is slower. It is because the matrix consumption is caused by the hot fluid movement, which travels slowly in the porous medium.

As we can see on figure 4.2d1, the hot fluid went less far from the heat source than in the original simulation. Furthermore, the swirls of the hot fluid are less pronounced. However, the encounter of the hot fluid with the boundary limit of the top wall has the same effect as in the original simulation and the heated fluid upward travel stops at the same height and finally the second plume travels less far upstream.

We can see on the figure 4.2d2 that the consumption of the porous medium also travels inward to the center and is less pronounced on the areas close to the pure-fluid interface. However, since the hot fluid travels at a slower speed in the material, more heat is convected away from the porous bloc in to the areas close to the pure-fluid interface. We can observe on the figure 4.2d2 that the shape on the iso-ϕ curves advance further from the heat source in the interface areas.

These differences in the behaviour of the hot fluid are mainly due to the fact that in the carbon combustion model, the constituents of the combustion products are different from the initial fluid. In the original simulation, it was assumed that the fluid phase always comprises a single chemical species. The porous material would burn to become the gas that was flowing in the channel as shown in the reaction (3.1). On the other hand, in the carbon combustion model, the products of the combustion are different from the gas flowing in the channel as we can see on equation (3.9).

The inflow gas is air (oxygen and nitrogen) and the combustion product is a mixture of nitrogen, carbon dioxide and, depending on the location in the domain,

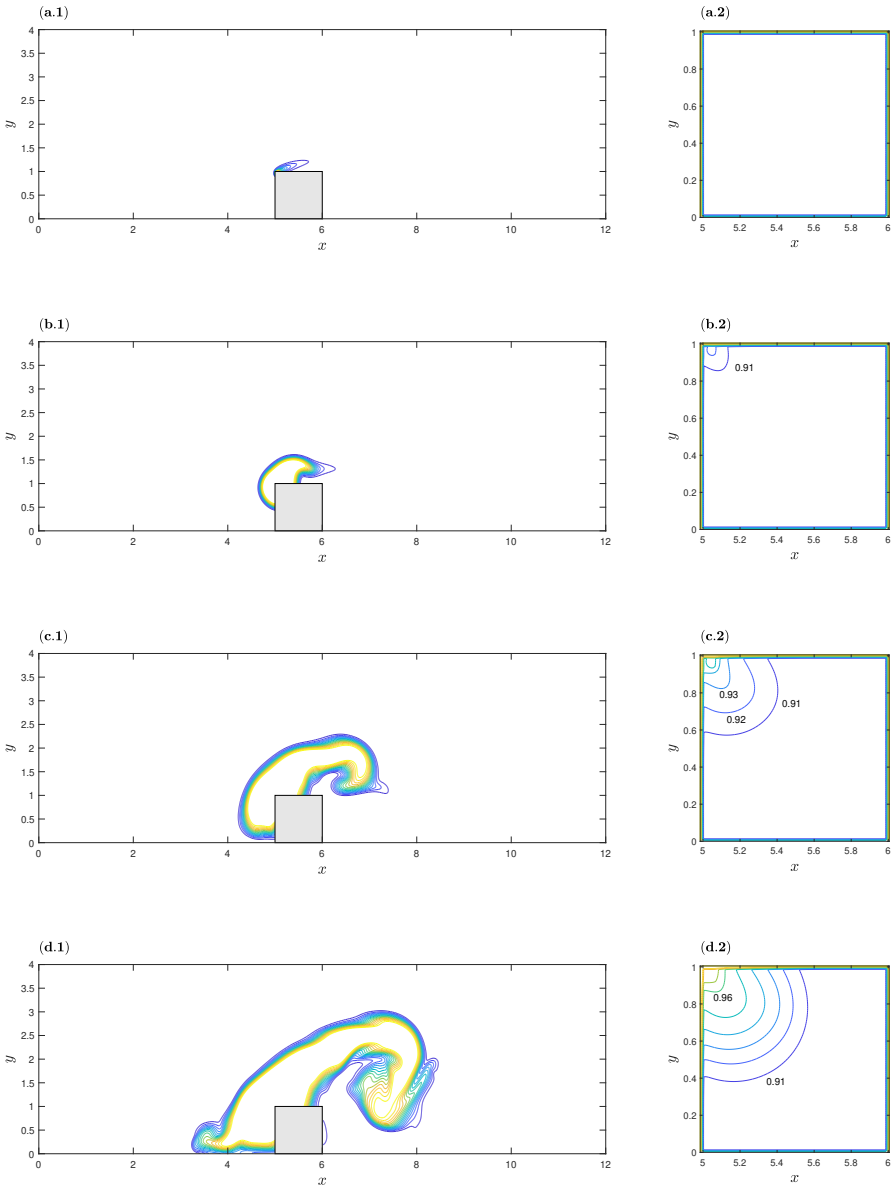

Figure 4.2: Carbon combustion model with spark ignition. Fluid-temperature field (left) and fluid volume fraction (right) at four instances during the evolution of the flow. (a) t = 1.46; (b) t = 2.0; (c) t = 2.85; (d) t = 3.86

oxygen. The mixture generated by the combustion has a higher molar mass than air, which means that the combustion product has a higher density than the air as we can see on figure 4.3.

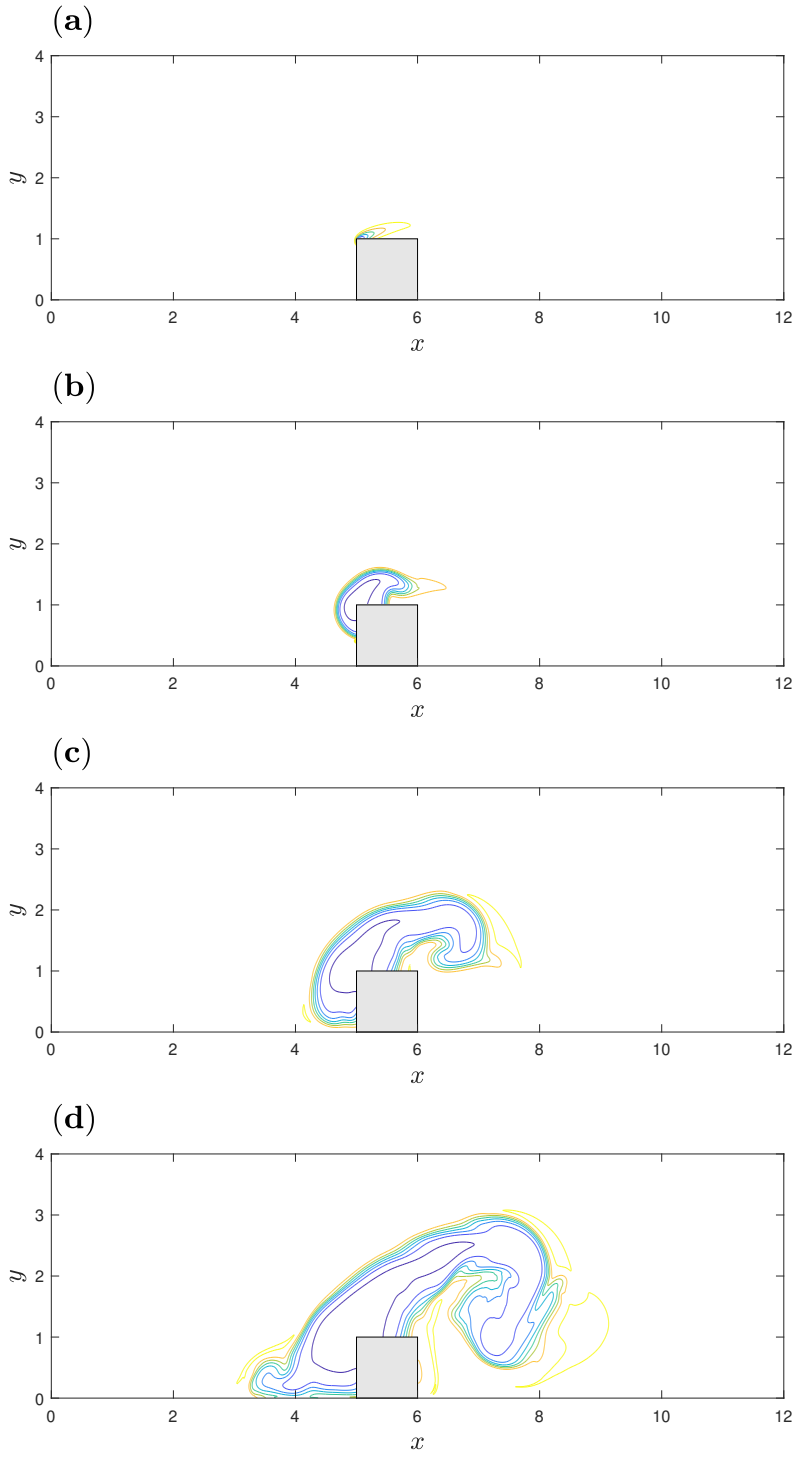

Figure 4.3: Carbon combustion with spark ignition simulation. Fluid density at the same four instances as in figure 4.2

Therefore, during the reaction, two phenomena occur in competition with each other. On one hand, the chemical reaction transfers heat to the fluid, increasing its temperature and expanding it and hence reducing its density. On the other hand, the heat is transferred into a mix of air and combustion products that has a higher density than air.

Regarding the propagation of the different gasses, we can see on the figure 4.4that at $t = 1.46$, the corner of the porous bloc is being heated by the heat source. The temperature is approaching $T = 3.5$ and therefore the start of self-sustained reaction. On figure 4.5, we can see the combustion front moving and following the movement of the high-temperature zone ($T > 1$). The oxygen meeting the combustion front is being burned. Furthermore, it can be observed that the mass concentration curves of the 2 gasses have the same shape. It is due to the fact that the formation of CO_2 involves the consumption of O_2.

On figure 4.6, we can also see that the CO_2 mass fraction increase front travels further downstream in the first plume and further upstream in the second plume than the high-temperature plumes. Consequently the mass fraction of O_2 decrease front. We can see on figure 4.7 that the zones of great concentration of CO_2 swirl. Since the carbon dioxide travels with the hot gas, it follows its movements and therefore swirls because of the reason detailed before.

During the evolution of the flow, there are some zones where the density of the fluid becomes greater than 1. On the figures 4.8-4.10, only the density above 1 have a thicker contour. This will allow us to observe the evolution of the high-density areas of the domain. On the figure 4.8, we can see 3 high density zones forming. The first one appears on top of the first plume, fitting the shape of the hot fluid ahead of its movement. The second one is upstream of the second plume, partially inside the bottom left side of the porous block. The third high-density zone is mainly located inside the porous medium. The figure 4.9 shows that the high-density regions move ahead of the hot fluid and grow with time.

Theses regions are due to the presence of combustion products in front of the hot gas. This generates zones where the density of the gas is increased by the products of the combustion before it is decreased by the heat emanating from the reaction. On the figure 4.10, we see that at $t = 3.9$ the high-density zones have continued to move ahead of their respective portion of hot fluid. The third high-density zone has completely left the highly porous bloc. Furthermore, a fourth high density region was formed and is located around $(x = 8l, y = 3l)$. It is moving downstream, in direction of the bottom wall, getting closer and closer to the third high-density region.

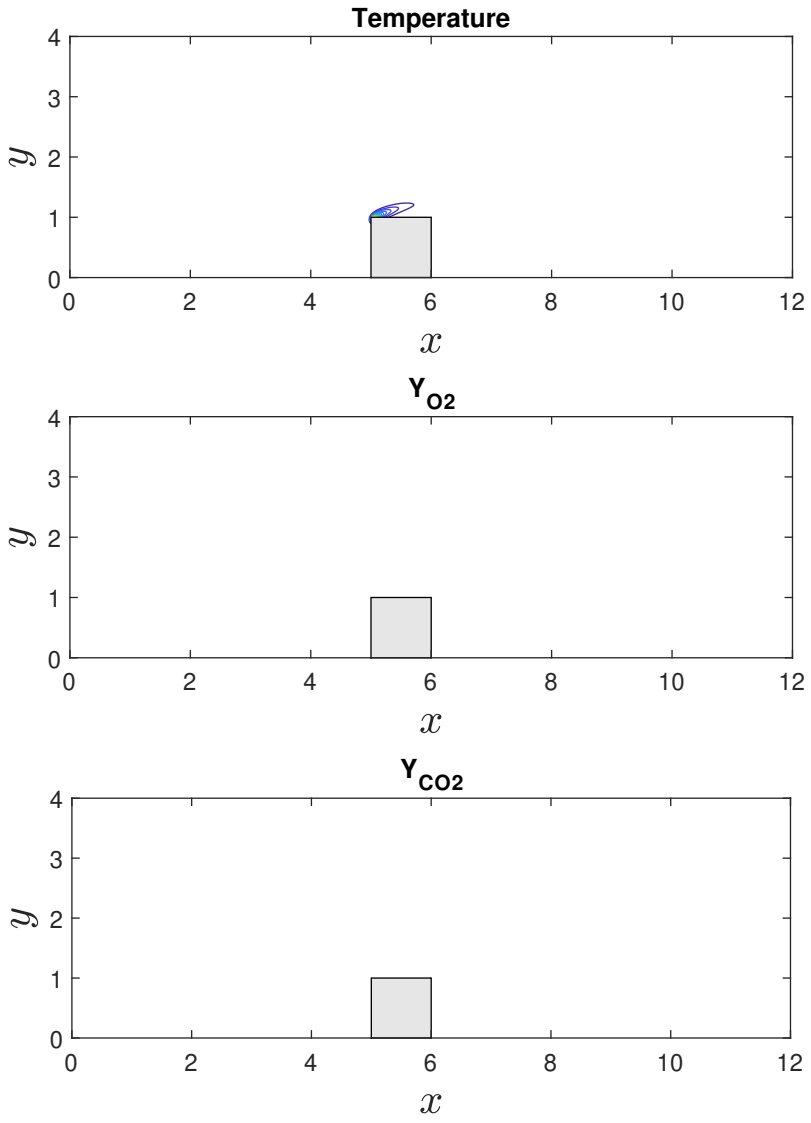

Figure 4.4: Temperature and mass fraction of gasses at t=1.46

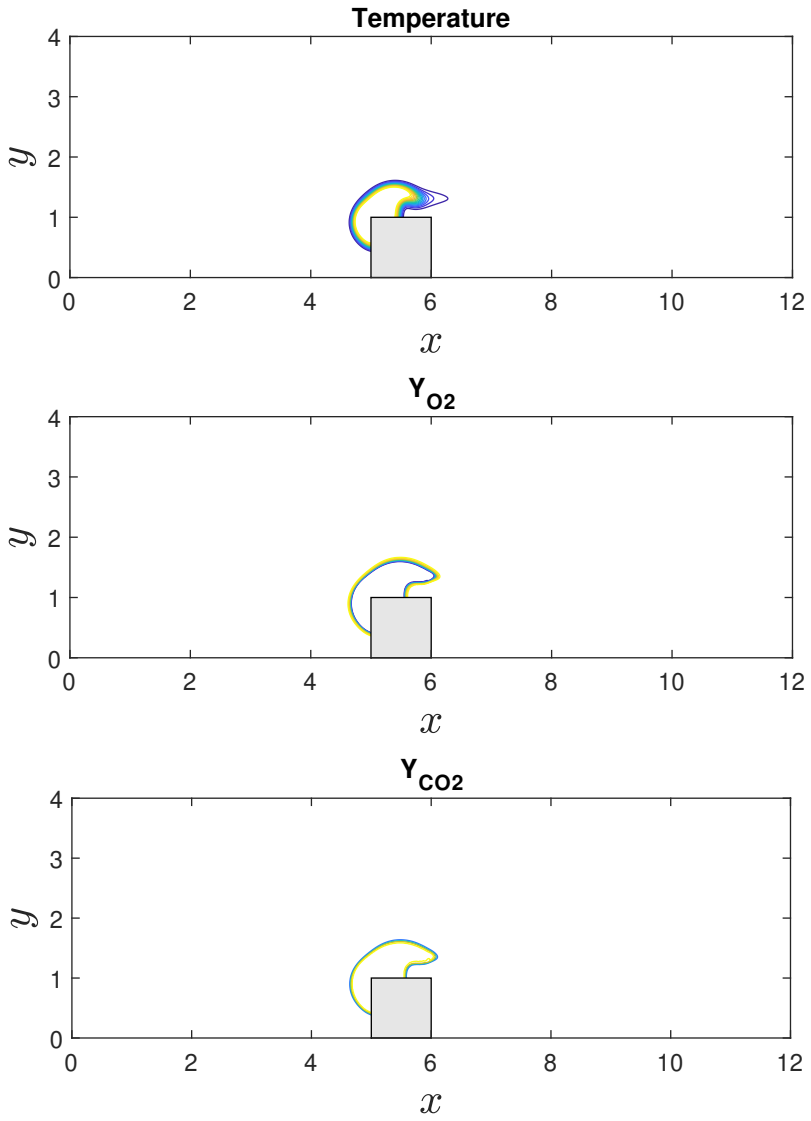

Figure 4.5: Temperature and mass fraction of gasses at t=2

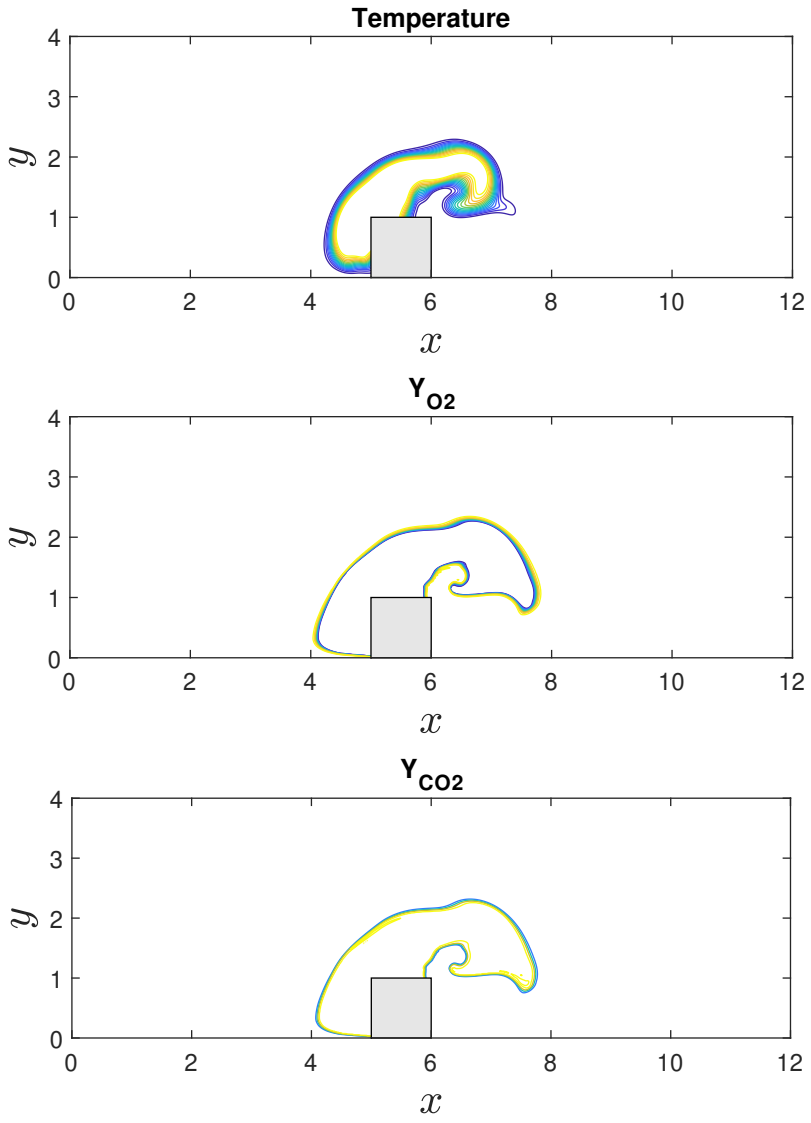

Figure 4.6: Temperature and mass fraction of gasses at t=2.85

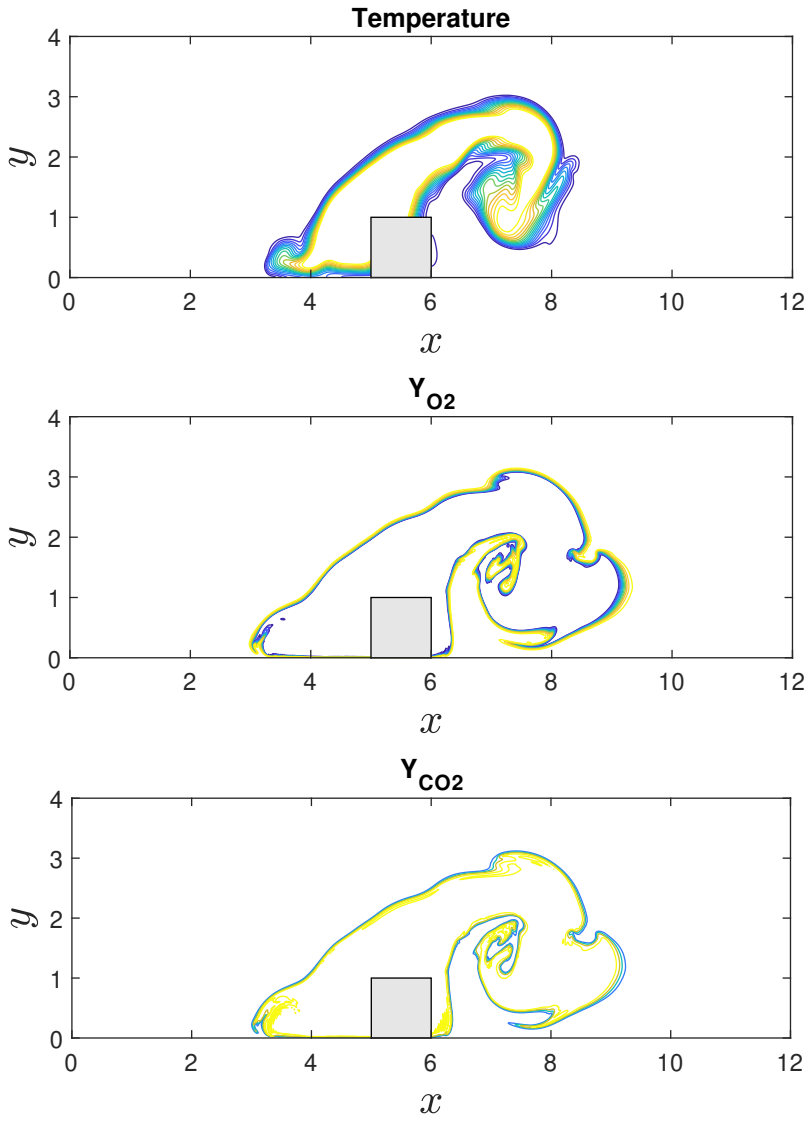

Figure 4.7: Temperature and mass fraction of gasses at t=3.86

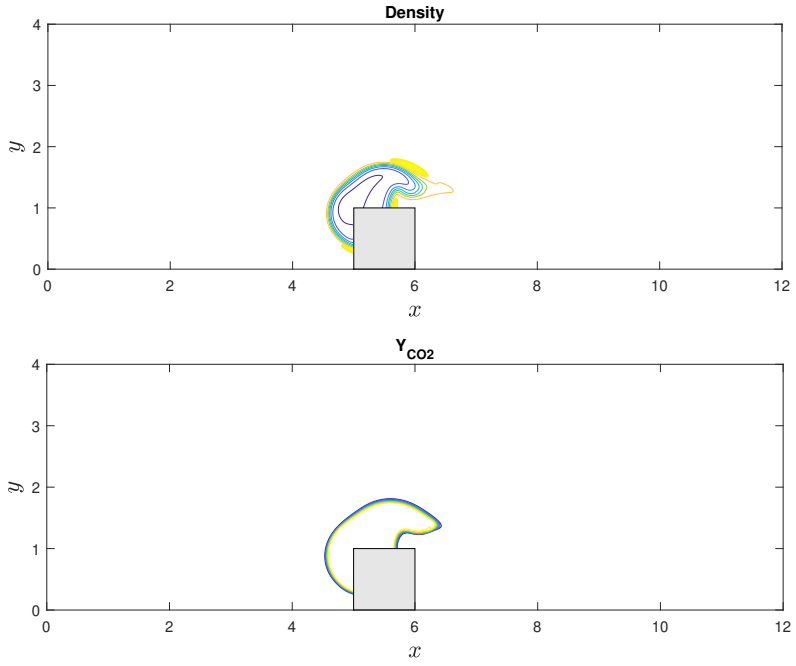

Figure 4.8: High density zones of CO_2 at t=2.1 High density zones have thick contours

4.4 Hot inflow ignition

4.4.1 Original resuls

Figure 4.11 shows the temperature and the porosity of the porous medium at 4 moments of the original simulation found in the thesis of Panagiotis [3]. At the beginning of the simulation, the hot fluid enters the domain and moves downstream towards the porous block. On figure 4.11a1, we see that the first layers of hot gas reaches the porous material at $t = 10.1$. The isotherm curves are asymmetrical with regards to the centerline a $y = 2$. It is due to the fact that the buoyancy forces push the hot gas upward to the upper part of the channel. Indeed, at this time, 49% of the mass flux at x=5 passes above the porous block, 32% passes bellow and 19% passes through its upstream interface.

As the hot fluid enters the porous medium, the temperature of the solid phase rises. However, the porous bloc temperature rises slowly. The thermal non equilibrium resulting from this temperature difference can be seen on figure 4.14.

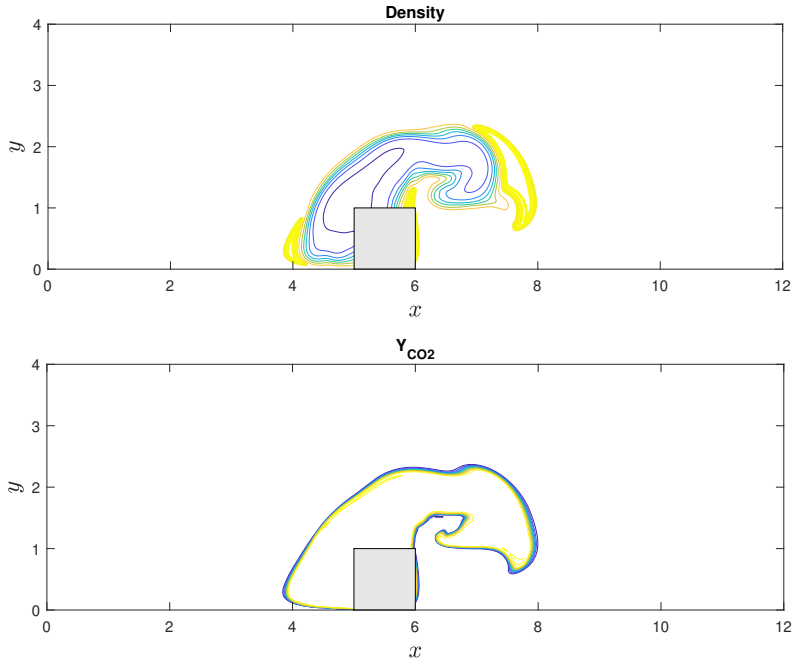

Figure 4.9: Density and mass fraction CO_2 at t=3

At this point, the temperature of the fluid inside the porous block is not high enough to induce a reaction. The porosity of the material stay unchanged (see figure 4.11a2). At around $t = 18.74$, the fluid temperature is high enough to start the reaction. From this instance, the evolution of the flow can be divided into two phases. A first phase that lasts until $t = 31.9$ during which the rate of reaction is slow. A second phase that lasts until $t = 37.55$ in which the reaction rate is fast.

During the first phase, the heat rejected by the reaction is absorbed by the fluid phase. The fluid temperature displays a steep drop in the streamwise direction inside the porous medium. We have a noticeable consumption of the portion of the solid phase near the heat source as we can see on figure 4.11b1. Due to interphasial heat transfer, the temperature of the solid block also rises. Nonetheless, it remains significantly lower than the fluid temperature as we can see on 4.14. Eventually, the hot gas temperature reaches a critical value which sets off a rapid increase in the reaction rate. This marks the start of the second phase.

During the second phase, we observe a rapid consumption of the porous block. This generates an important heat release that leads to the rapid expansion of the surrounding fluid. As we can see on figure 4.11d1 that the main body of the hot

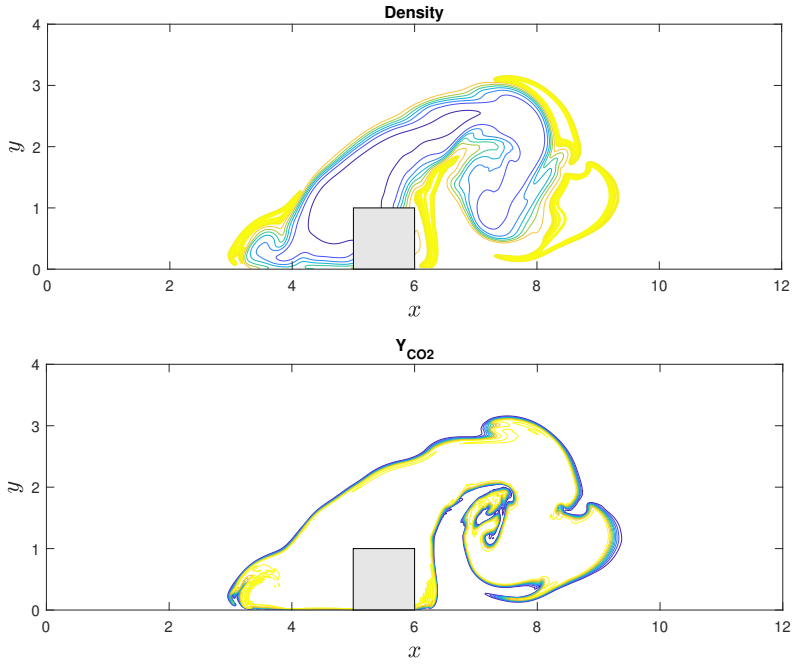

Figure 4.10: Density and mass fraction of CO_2 at t=3.9

fluid travels upstream. However, a significant part of the fluid flows towards the sides of the porous block and is drifted downstream. Furthermore, the fluid swirls on each side of the porous medium followed by a short reverse flow downstream of it as is typical in flows around bluff bodies. The combustion of the porous block during the second phase is more pronounced close to its center than it is close to its top and bottom sides.

4.4.2 Carbon combustion model results

We are now going to analyse the results of the same experiments using the carbon combustion model presented in section 3.4. As we can see on figures 4.13a1 and 4.13a2, the temperature field is the same as in the original simulation before the rapid reaction that starts around $t = 31.9$.

During the fast reaction rate phase of the combustion, we can see on the figure 4.13c1 that the hot gas zone of the flow growth is slower than in the original simulation. However, the difference in the expansion rate of the hot gas between

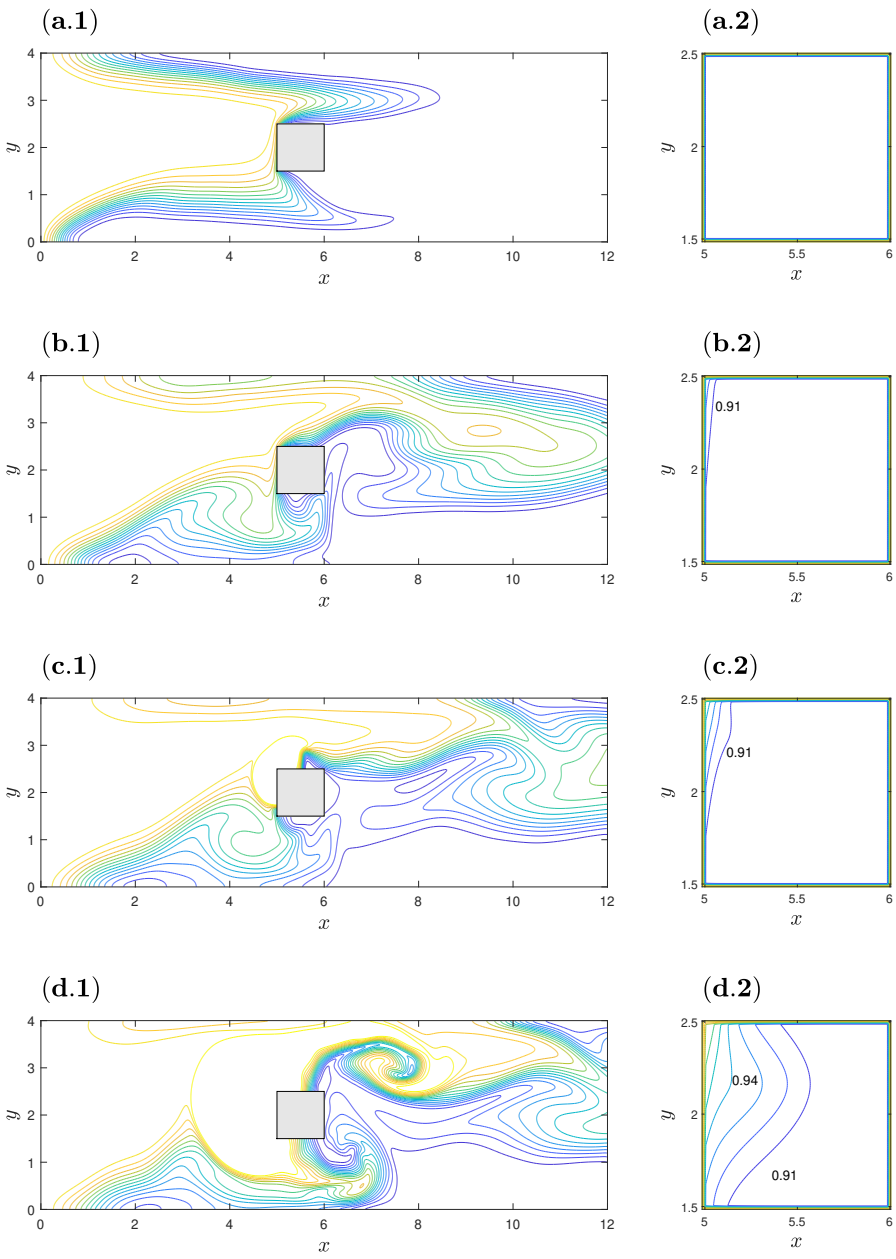

Figure 4.11: Original simulation of the burning porous block placed at the centerline of a pure-fluid channel. Fluid-temperature field (left) and fluid volume fraction (right) at four instances during the evolution of the flow. (a) t = 10.1; (b) t = 27.1; (c) t = 32.67; (d) t = 34.07

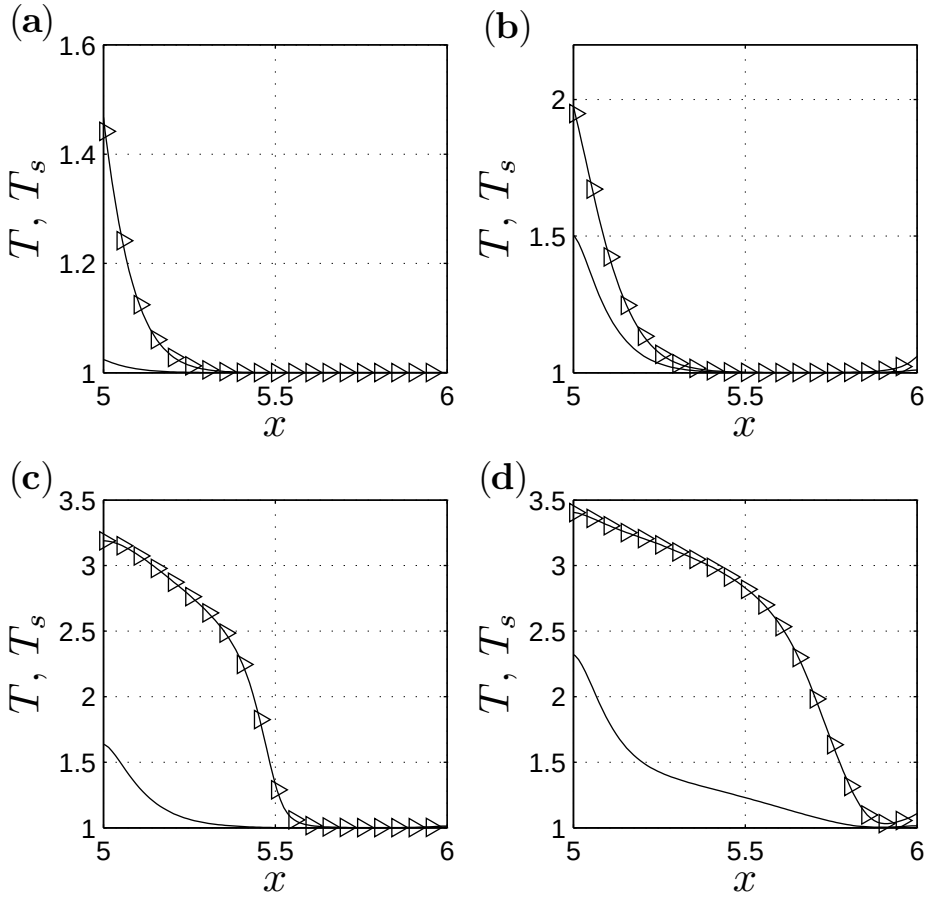

Figure 4.12: Original simulation of a burning porous block placed at the centerline of a pure-fluid channel. Profiles of the phasial temperatures at the channel centerline. The times that correspond to the plots are the same as in Figure 4.11 (▷) marks the fluid temperature and (-) marks the solid temperature. [3]

the initial simulation and the carbon combustion model is less pronounced than in the spark ignition experiment. Furthermore, as we have seen before, on the lower and upper wall of the channel, 2 hot gas vortices are generated due to the interaction of the hot expanding gas and the boundary layer of the walls. By comparing the figures 4.11d1 and 4.13d1, we can see that in this simulation, the lower and upper vortices are weaker. They advance less far and have smaller vorticities. Moreover, the upward going part of the hot gas undergoes a slower travels than in the initial simulation.

Similarly to the temperature field, the porosity fields are the same as in the original simulation before the start of the fast reaction rate phase as can be seen of figures 4.13a2 and 4.13b2. Comparing the figures 4.11c2 and 4.13c2, we can see that at the beginning of the fast phase of the combustion, the consumption of the porous block has similar profiles. They both start from the top left corner of the solid matrix and travels inward in the direction of its centre. However, the burning process is slightly slower in the carbon combustion model.

Before the fast reaction rate phase of the flow, the density field of the flow is the same in the original simulation and in the carbon combustion simulation. The increasing temperature of the inflow flux of hot oxidizer decreases its density. As we can see on figure 4.15a, we have an air inflow with a monotonously decreasing density that enters the domain through the left boundary. Furthermore, due to buoyancy effects, a greater proportion of low density (i.e. hot) fluid flows the zone above the porous medium as we can see on figure 4.15b. At $t = 15.27$, 46% of the hot fluid flows above the porous matrix, 32% flows inside it and 22% flows bellow the porous bloc.

On figure 4.16, we can once again see that the expansion rate is slower in the carbon combustion model. The reasons of this phenomenon have been explained in the section 4.3. Furthermore, like in the spark ignition model, we observe some higher density zone around the coordinates $(x = 5.5, y = 1.5)$. Contrary to the carbon combustion simulation, in this case, the higher density area disappears much faster at $t = 32.92$.

Regarding the propagation of combustion products, we have a similar behaviour than for the spark ignition simulation. The increase in the CO_2 concentration profile fit the decrease in the O_2 concentration profile. This is due to the fact that the oxygen in the air is consumed by the reaction to produce carbon dioxide. As we had observed in section 4.3, the mass concentration of the gasses follows the path similar to the one the hot gas (see figure 4.18). However, the areas of cold air containing CO_2 are much lower and exist for shorter periods of time. This results

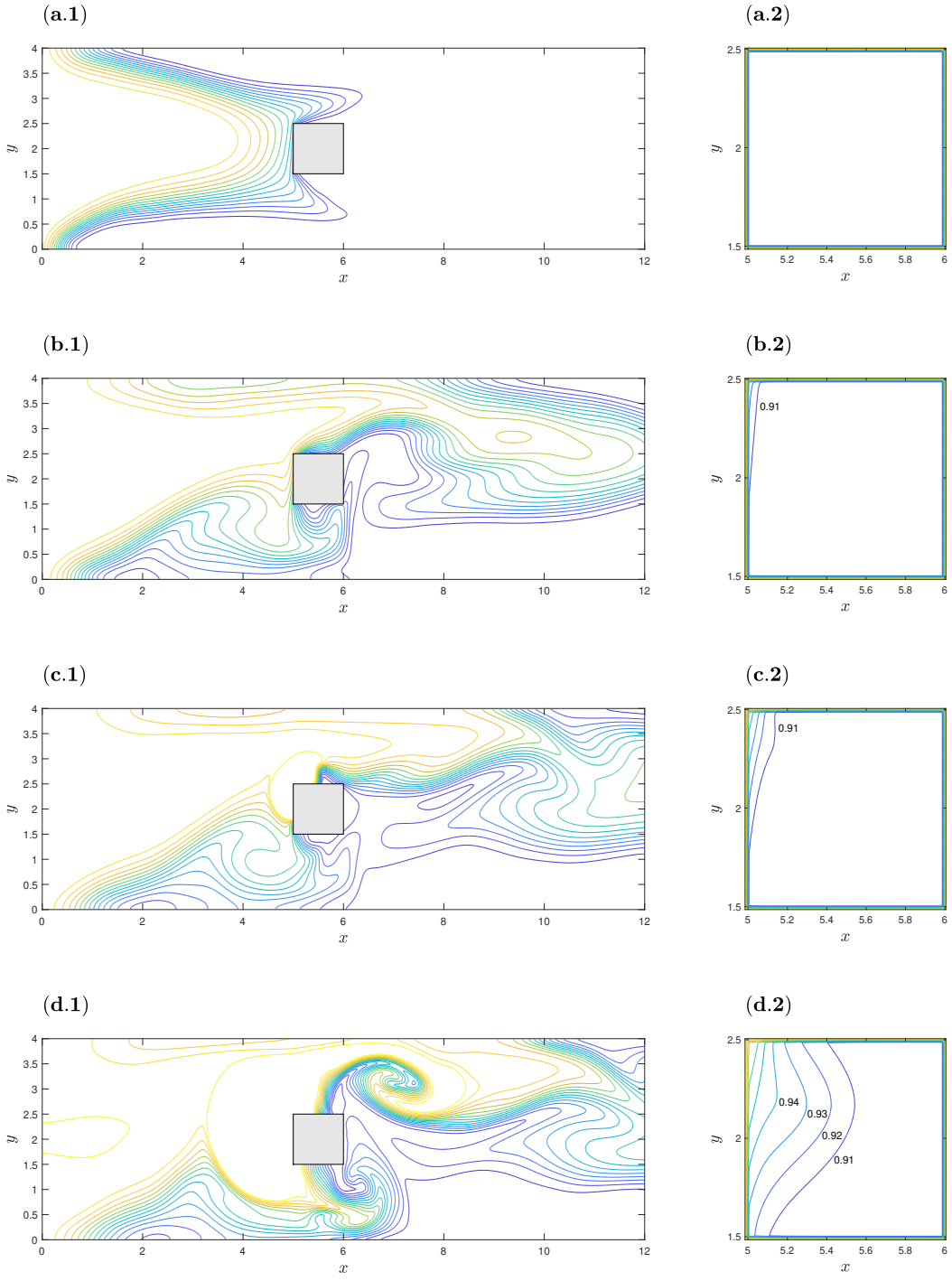

Figure 4.13: Carbon combustion with hot inflow ignition simulation. Fluid-temperature field (left) and fluid volume fraction (right) at four instances during the evolution of the flow. (a) t = 10.1; (b) t = 27.1; (c) t = 32.69; (d) t = 34.07

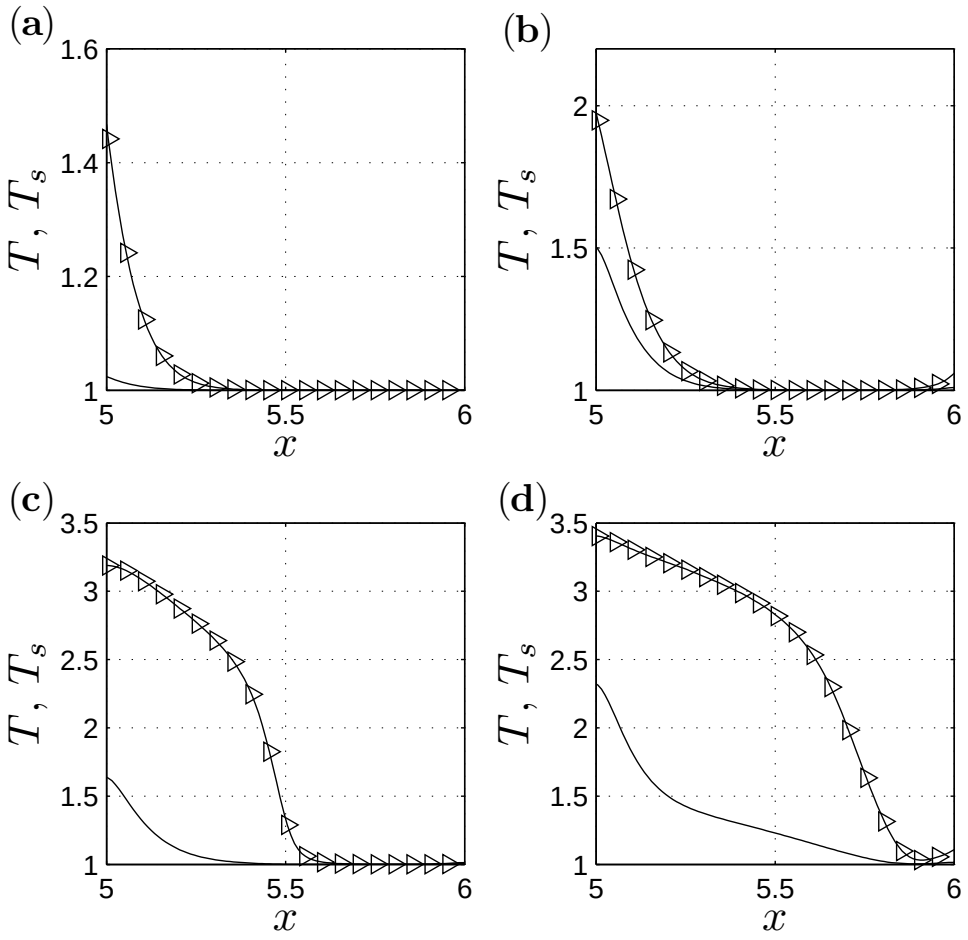

Figure 4.14: Original simulation of a burning porous block placed at the centerline of a pure-fluid channel. Profiles of the phasial temperatures at the channel centerline. The times that correspond to the plots are the same as in Figure 4.11 (▷) marks the fluid temperature and (-) marks the solid temperature.

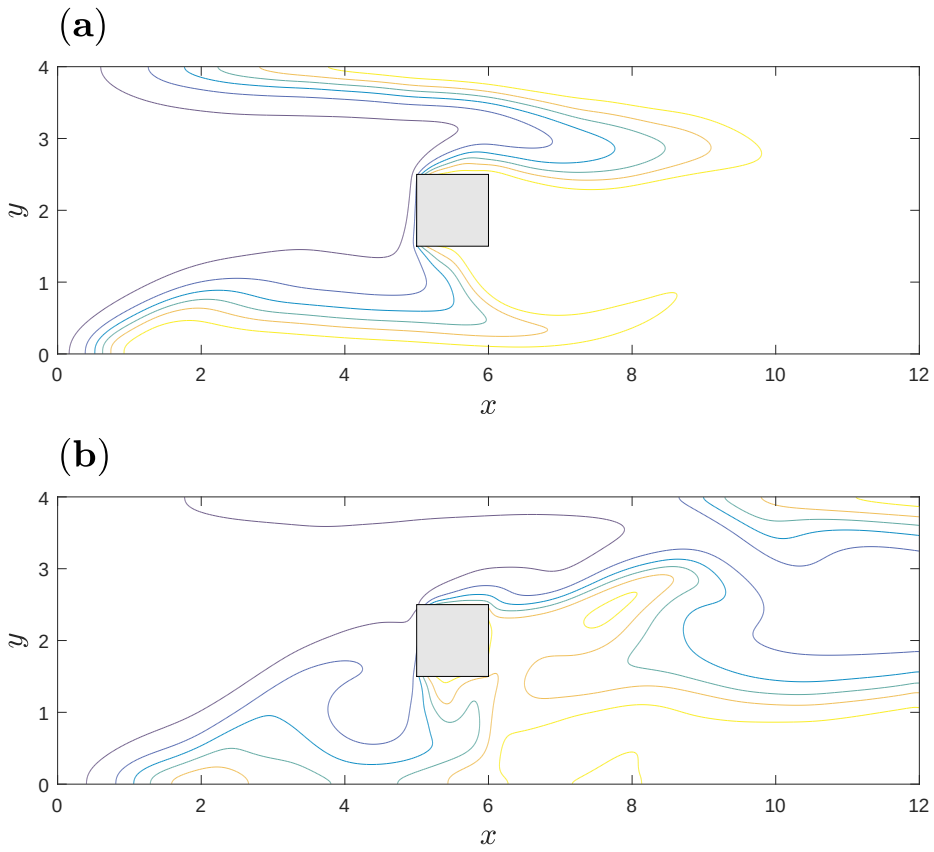

Figure 4.15: Simulation of the burning porous block placed at the centerline of a pure-fluid channel. Fluid density before the fast combustion. (a) t = 15.27; (b) t = 31.13

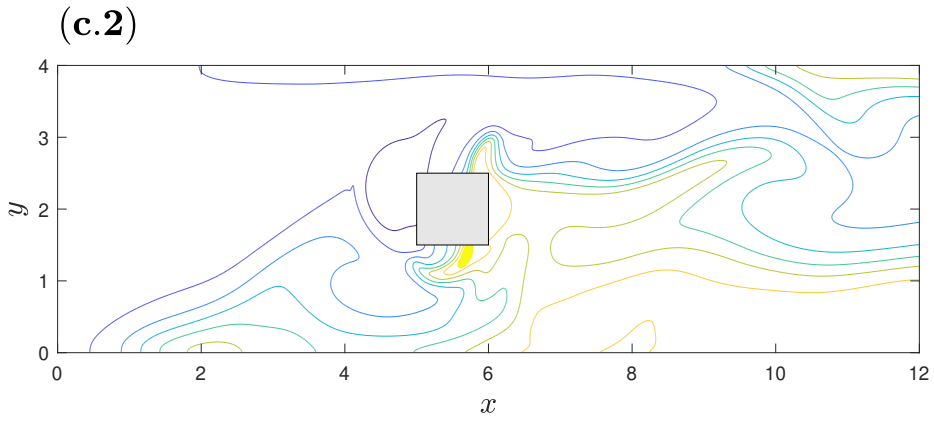

Figure 4.16: Fluid density before the fast combustion at t = 31.13. The higher density zone is highlighted

in less high-density zones (i.e. where $\rho > 1$) that last shorter periods of time, as we have seen on figure 4.16.

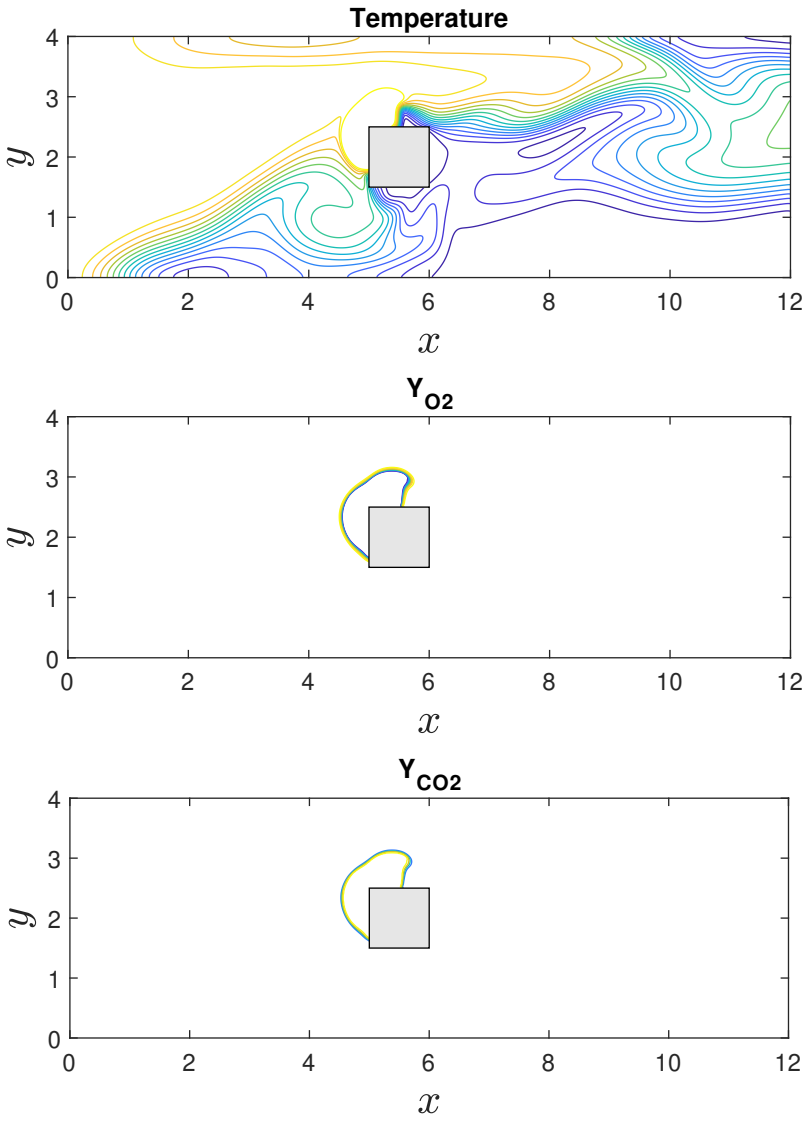

Figure 4.17: Temperature and mass concenstration of gasses at $t = 32.69$

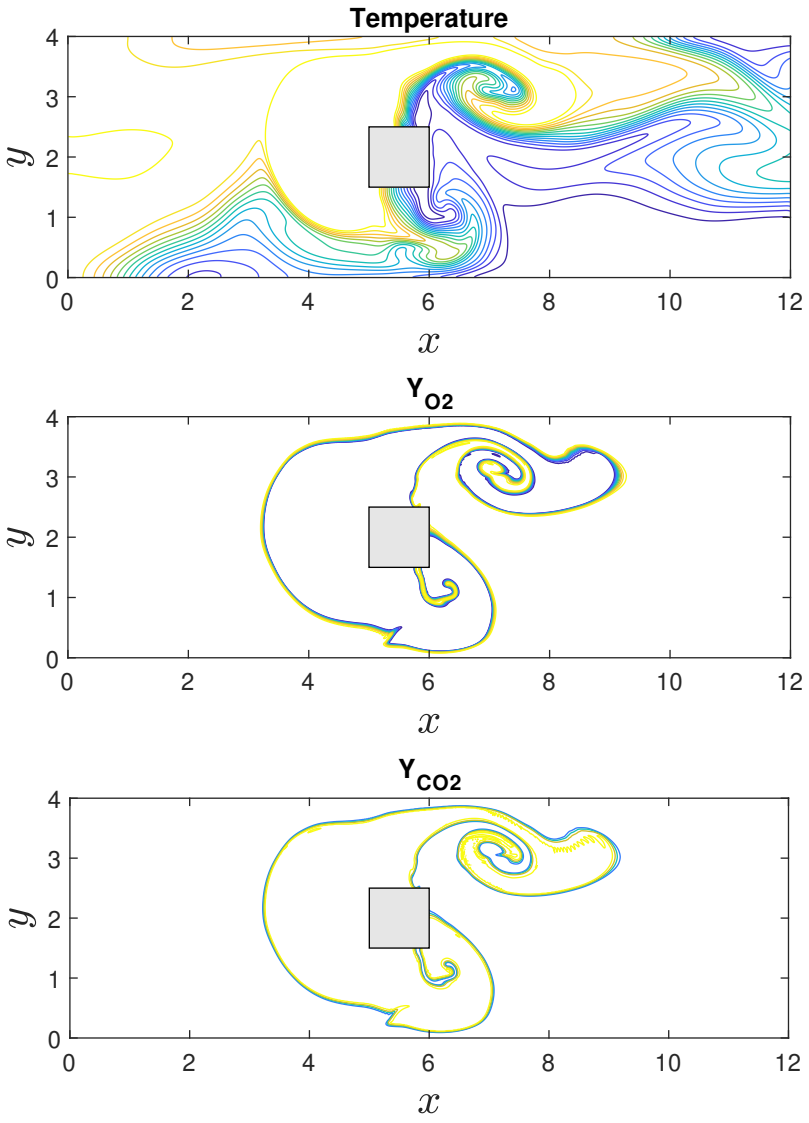

Figure 4.18: Temperature and mass concenstration of gasses at $t = 34.07$

Chapter 5

Burning of canopy

5.1 Introduction

Predicting the behaviour of flames in canopy fires is important for the study of forest fires spread. It is essential in the design of efficient fire management and fire suppression policies.

The burning of vegetative fuels emits a complex mixture of particles and gases into the atmosphere. The precise composition of the combustion products depends on a wide range of variables (vegetative fuel types, wind speed, initial temperature, etc.). The burning of the canopies releases into the atmosphere the carbon stored during photosynthesis and other often toxic compounds. The ability to forecast the concentration and position of those potentially harmful combustion products is a hard but critical challenge. In this chapter, the model presented in section 3.5 is used to simulate a combustion on a canopy placed on the ground.

In section 5.2 the set-up of the simulation is detailed, in section 5.3 the results of the simulation are presented and finally, in section 5.4 the results are discussed.

5.2 Simulation set-up

In this model, the forest canopy is assimilated to a porous block. The goal is to simulate the combustion of the porous medium. Its dimensions in the streamwise

$\hat{l}_{ref} \quad [m]$	$7.8 \cdot 10^{-3}$
$\hat{u}_{ref} \quad [m/s]$	1
$\hat{T}_{ref} \quad [K]$	300
$\hat{\rho}_{ref} \quad [kg/m^3]$	1.117
$\hat{\mathcal{R}}_{ref} \quad [cal/(mol\ K)]$	1.987

Table 5.1: Reference values of the forest fire model

and cross-stream directions are $l_x = 4l$ and $l_y = l$. The initial porosity of the porous medium is $\phi^0 = 0.84$ which is according to [6] a good approximation for the porosity of a forest canopy. Furthermore, the dimensions of the domain in the streamwise and cross-stream directions is to $L_x = 12l$ and $L_y = 4l$ respectively. The porous medium is placed on the bottom wall of the domain. Along the streamwise direction, it is placed from $x = 4l$ to $x = 8l$.

At the start of the simulation, the domain is isothermal and the 2 phases are in thermal equilibrium. Assuming that the reaction 3.13 has similar Arrhenius parameters as the following reaction

$$\mathrm{CHO} + \mathrm{O_2} \longrightarrow \mathrm{H_2O} + \mathrm{CO} \tag{5.1}$$

according to [23] and after non-dimentionnalisation we obtain the following parameter for the formula (3.2) : $K_R = 41.59$, $E = 11.67$. The reference values of the model are changed to emulate a more realistic situation. Their value are given in table 5.1.

From these values, we can see that the values of the Reynolds and Richardson number are different from the carbon combustion model. In this simulation, we have $Re = 500$ and $Ri = 0.677$. However, since the Prandtl number is only dependant on the fluid's intrinsic properties, it is unchanged $Pr = 0.71$.

This simulation models a fire occurring on a canopy directly placed on the ground with a small wind of $u = 1$. The bottom boundary of the domain, which represents the ground, is modelled as a wall. The top and right boundaries are modelled as open domains. Since we are modelling phenomenon close to ground altitude, we can neglect the variation of the streamwise speed with the height due to the atmospheric boundary layer. Therefore, at the left boundary we have a constant inflow uniform air inflow of speed $u = 1$.

To obtain the initial velocity conditions (u, v), a preliminary run of an isothermal pressure-driven flow is performed. The obtained initial velocity field is applied as the initial condition of the main simulation. The ignition is started the same way

it is done in section 4.2. A heat source is applied on a real of dimension $0.08l$x$0.08l$ at the upper upstream corner of the porous strip, until $t = 1.6$.

5.3 Simulation results

At the beginning of the simulation, the upstream top corner of the porous medium is heated. This heat is transferred to the fluid and increases its temperature. A part of the hot fluid is then convected downstream, driven by the establish flow around and through the porous medium. At $t = 1.17$, the temperature at the corner of the porous material reaches $T = 3.5$ which starts the combustion process as we can see on figure 5.1a. At this moment of the simulation, the porous medium is left intact (see figure 5.2a).

The gas surrounding the heat source starts expanding due to the rapid increase of heat transferred to it by the fast combustion reaction. We can see in the figure 5.1b that the hot gas that goes into the porous matrix travels diagonally in it in direction of the ground. An important part of the hot gas is pushed upward due to buoyancy effects and encounters the inflow hot cooled air. This creates a small but noticeable swirl downstream and above the heat (visible on $(x = 5, y = 1.5)$ on figure 5.1b). Furthermore, a small part of the hot gas travels upstream. At this stage, a small part of the porous medium starts to be consumed. As we can see on the figure 5.2b, the porosity profiles follow to a certain extent the diagonal going from the top-left of the porous medium to $x = 4.5$.

At $t = 1.6$, the heat source stops. The flow continues to evolve in the 3 directions stated before. Furthermore, the hot gas at $T = 3.5$ that was on the top upstream corner moves in the above-upstream direction and can be seen on the figure 5.1c at $(x = 4, y = 1.5)$. We can also see on the figure 5.2c that the burning of the porous medium progresses diagonally in the direction of the ground.

Without a source to transfer heat to the hot gas, its temperature decreases while it expands. We can observe on figure 5.1d that the "pocket" of gas that left the corner of the porous medium expands and experience a temperature decrease. The continuing expansion of the hot fluid increases the size of its swirl. Indeed, the interaction with the rising hot gas and the uniform inflow air pushes the hot air downstream but also generates growing vortices that can be seen on figure 5.1d at $(x = 6, y = 2)$. Moreover, the hot fluid travels further downstream of the porous medium. However, inside the porous medium, the hot fluid stops advancing around $x = 5$.

Furthermore, observing the iso-thermal curves on the figure 5.1d show us how the fluid flow is faster outside the porous medium that it is inside it. At $t = 2.45$ at around $(x = 4.4, y = 0.2)$, a small bubble of the porous medium undergoes a stronger consumption by the heated fluid. We can see on figure 5.2d that the higher porosity zone grows. At the same time, another higher porosity area is created at the top-left corner.

Regarding gas products of the combustion, even though their mass concentration is different, their propagation is extremely similar. Their propagation fit the movement of the hot fluid for reasons that were stated in earlier chapters. The concentration curves of the carbon monoxide can be seen on figure 5.3.

5.4 Discussion

In this section, the reference values and non-dimenstionnal numbers were chosen to mimic a small portion of the canopy in the open-air. In the simulation, the incoming wind speed is 1 $[m/s]$ (3.6 $[km/h]$) and we have $l = 1$ $[m]$. This gives us a domain of 12x4 $[m]$ and a canopy of 4x1 $[m]$. Furthermore, we supposed that the ground acted like a wall and that the canopy was directly on the ground. Therefore, neglecting the influence of the influence of the trunk and roots of trees in the combustion.

The behaviour of the hot gas resultant of the combustion reaction is what we would expect from fire smoke. Indeed, various experiments of fire conducted outside with small will velocity lead to behaviours that are similar to the one observed in the simulation. The hot gasses are pushed upward due to buoyancy forces are some swirls are observable downstream as we can see in the experiment conducted on figure 5.4. The low wind speed in our simulation allowed stronger swirl to form.

Regarding the reaction initiation process, in the simulation, the application of heat source on the canopy generates a fast combustion process that can be assimilated to a deflagration. The heated gas expands quickly in multiple directions. This is not the typical behaviour of a fire in a canopy started by a heat source.

In the simulation, we supposed that the reaction was a single-step. Furthermore, we assumed that its products we uniformly distributed in the fumes. After the start of the combustion, the reaction products mass fraction increase until reaching their saturation concentration.

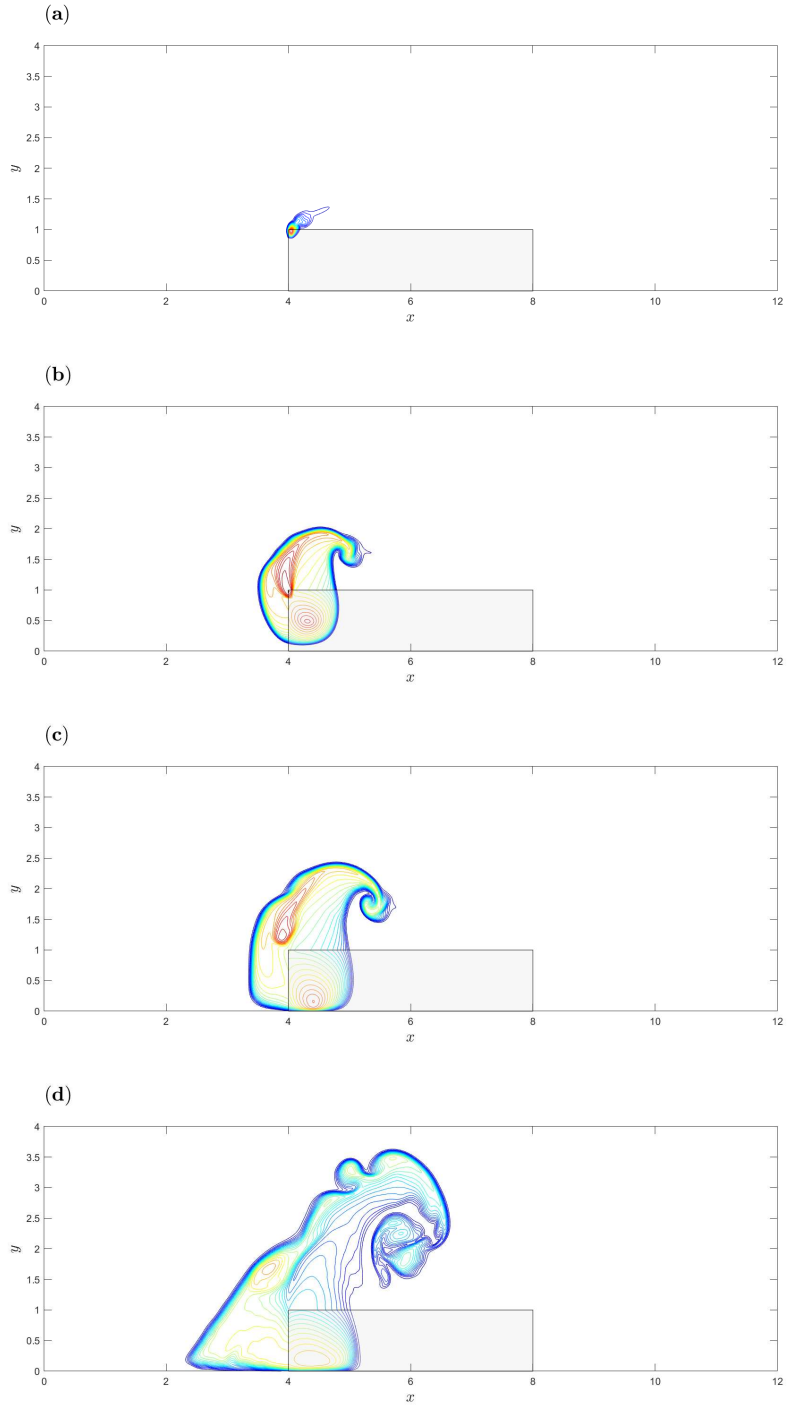

Figure 5.1: Forest fire simulation : Fluid temperature at four instances during the evolution of the flow. (a) t = 1.17; (b) t = 1.57; (c) t = 1.73; (d) t = 2.51

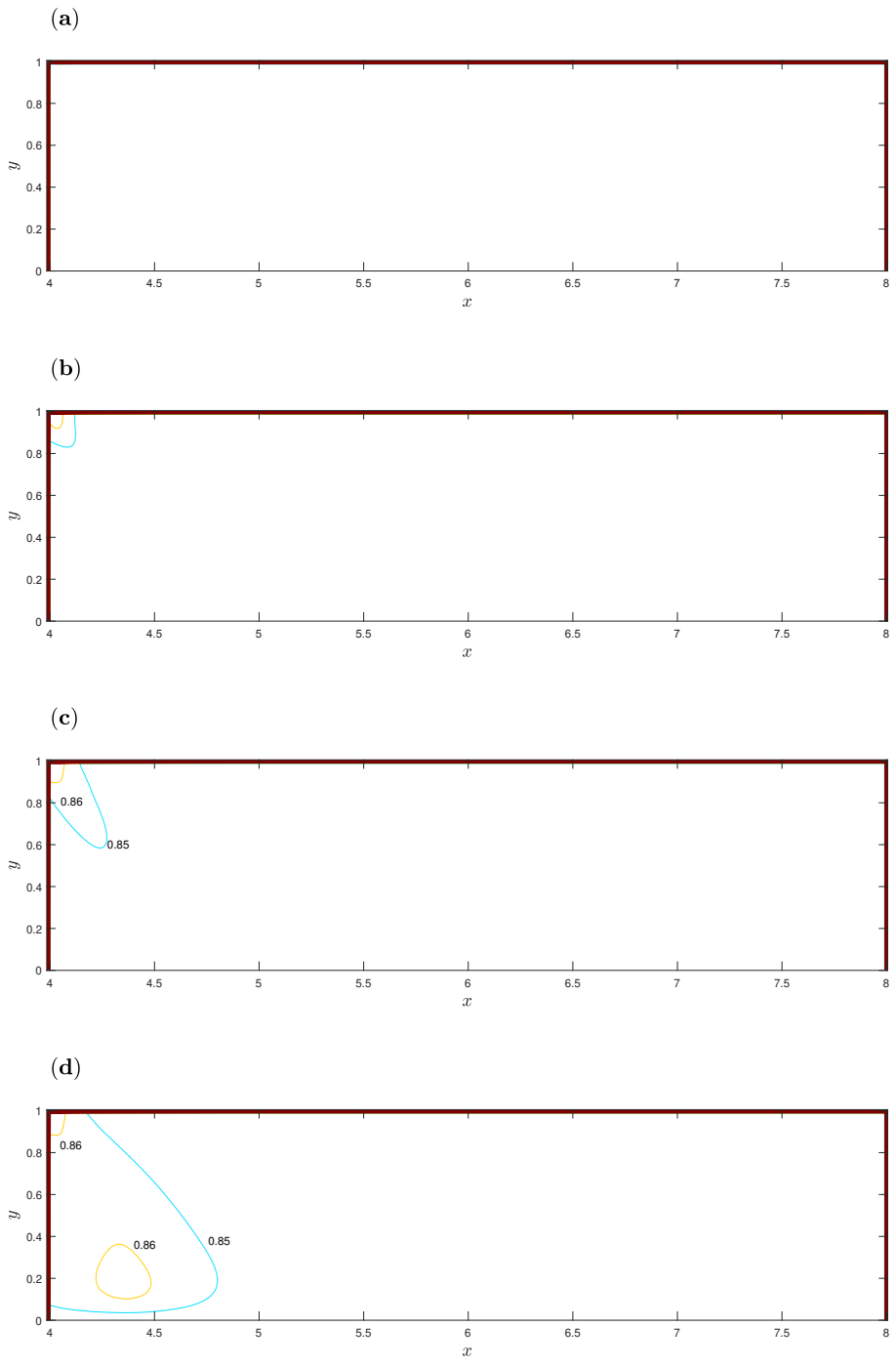

Figure 5.2: Forest fire simulation : Fluid volume fraction. The times that correspond to the plots are the same as in Figure 5.1

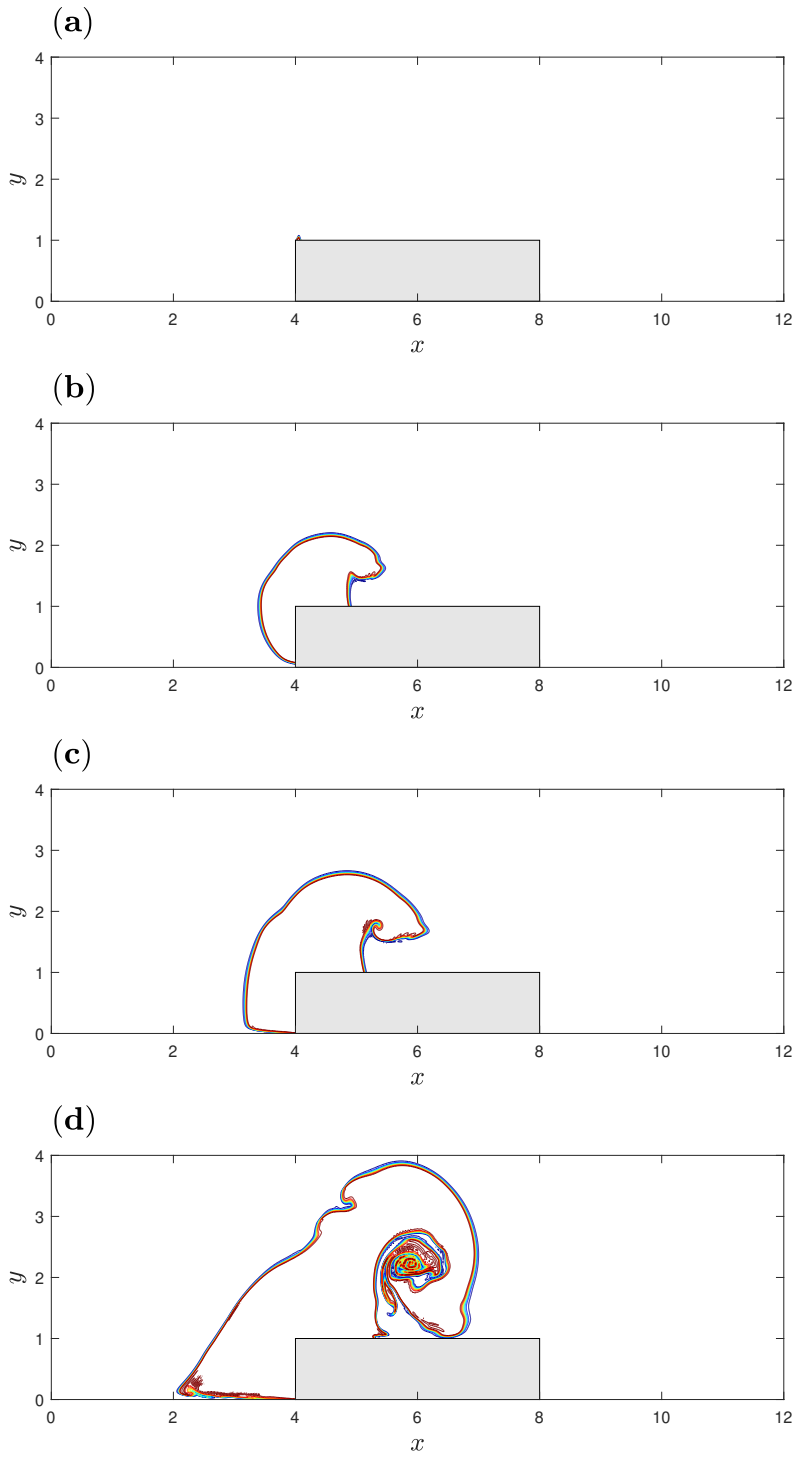

Figure 5.3: Forest fire simulation : Mass concentration of combustion carbon monoxide at the same times as in figure 5.1

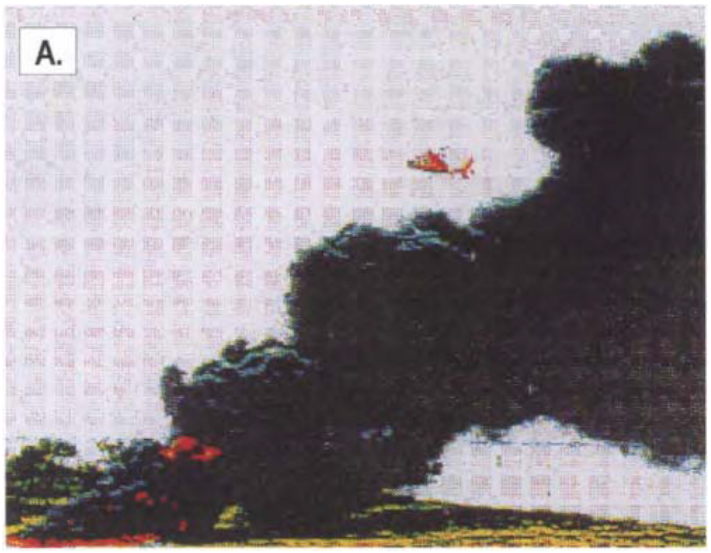

Figure 5.4: Diesel oil pool fire using a 15-m square shape open-top container (Test conducted by the Building and Fire Research Laboratory at the National Institute of Standards and Technology, at the U.S. Coast Guard Fire and Safety Test Detachment in Mobile, AL).

The final values of the gasses in the combustion smoke can be seen on table 5.2. The mass concentration of carbon dioxide and carbon monoxide deppend on the combustion efficiency. These parameters depends on multiple factors (tree type, air velocity, excess air levels, i.e). When comparing the emission of combustion of broadcast burns of logging (see figure 5.5) we can see that we obtain similar results. However, we usually obtain a much lower mass fraction of NO_x in practice. Even though the value also varies with atmospherical conditions and the type of tree burned, according to [11], the mass fraction of NO_x from tree combustion is around 0.00035.

specie	mass fraction [/]
O_2	0
N_2	0.6796
CO_2	0.226
CO	0.0178
H_2O	0.0757
NO_2	0.0009

Table 5.2: Mass fraction of the smoke

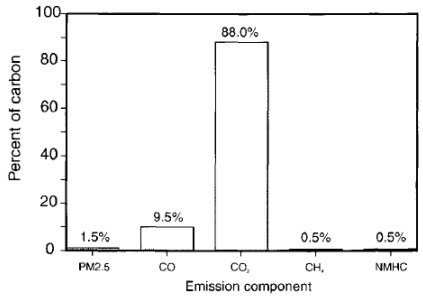

Figure 5.5: The average distribution of carbon between the primary products of combustion for broadcast burns of logging slash in the Pacific Northwest in the United States. [16]

It is important to note that practical fluid flow in caponies are not laminar, they are turbulent. The flames emanating from theses flow are also turbulent. Furthermore, in this model, we supposed that all the combustion products where gaseous. In reality, the burning of vegetative fuel generates Volatile Organic Compounds (VOCs).

Due to the limit in the value of the Reynolds number of this model, performing big-scale simulations of realistic forest canopies (i.e. porous medium having several $[km]$ length) is not possible in an acceptable period of time.

Chapter 6

Conclusion

In chapter 2, the mathematical model was developed in [3] and its corresponding numerical applications were briefly described. In chapter 3 the combustion model used in this work was explained, in chapter 4, this model was applied to a classical chemical reaction: the complete combustion of carbon. The numerical simulations of combustion presented in [3] were performed again using this time the new combustion model. Finally, in chapter 5 a fire occurring on a canopy was simulated.

In the initial model of Panagiotis [3], the combustion is assumed to convert the solid matrix into the same fluid that flows in the pure-fluid part of the domain. Taking into account the formation and propagation of the combustion products allowed us to observe the influence they have on the flow around a fire in a porous medium. Indeed, the mass fraction of the combustion products in the smoke determines its density and therefore its response to a heat influx. We observed in chapter 4 that the mix of air and carbon dioxide that constitute the smoke had a higher density than air. The heat transferred in the hot gas resulted in a smaller expansion. Furthermore, the presence of CO_2 in non-heated area generated some zones where the density was higher than the one of the incoming air.

Simulations of fluid flow, heat transfer, and combustion on a porous medium can be used to approximate real behaviours in canopies. However, as we observed in chapter 5, the equations and algorithms used in this work are made for flows with small Re. This limitation renders big-scale simulation of forest canopy fire impossible to be performed with an acceptable computing time. Furthermore, in practice, flows inside forest canopies are not laminar, they are turbulent and so are the flames.

While not being able to perform a satisfactory simulation of a fire in a canopy, the combustion model developed in this thesis produces more realistic results.

Appendices

Appendix A

Derivation of the mathematical model

Thermo-mechanical model

Let $\Omega \subset \mathbb{R}^3$ be an open and bounded domain that contains both saturated porous and pure-fluid regions. The porosity distribution $\phi(\boldsymbol{x}, t)$ is introduced as a concentration parameter that measures the density of volume occupied by the fluid According to [5], $\phi(\boldsymbol{x}, t)$ is a probability density function defined in Ω and take values in the interval [0,1].
Let $\Omega_p \subset \Omega$ be the subdomain that is covered by the porous material, $\Omega_p = \{\boldsymbol{x} \in \Omega : \phi(\boldsymbol{x}, t) < 1\}$. Similary, let $\Omega_p \subset \Omega$ be the subdomain that is covered by pure fluid, $\Omega_f = \{\boldsymbol{x} \in \Omega : \phi(\boldsymbol{x}, t) = 1\}$. Also, let S_{Ω} denote the boundary between Ω_p and Ω_f. Since Ω_p is an open subset of Ω, along S_{Ω} we have that $\phi(\boldsymbol{x} \in S_{\Omega}, t) = 1$.
The assumptions of our model are based on the following :

1. Each phase is modelled as a continuum thermodynamic system.
2. The two thermodynamic continua are immiscible but occupy the same space. In particular, they fill completely the space that they occupy (saturation condition).
3. The two thermodynamic continua are open to each other and at non-equilibrium.
4. The mass, momentum and energy exchanges between the two continua are pure, i.e. their sum must vanish.

5. The skeleton (or matrix) of the porous material is assumed to be a rigid solid of zero velocity and constant mass density. Also, the fluid is assumed to be simple and isotropic.

6. The postulate of phase separation holds. In other words, irreversible phenomena associated with only one phase do not depend on the variables of the other phase.

The two thermodynamic systems can interact with each other, these interactions are in the form of mass, momentum, and energy exchanges, and are denoted by $\mathcal{M}$, $\boldsymbol{f}$, and $\boldsymbol{\varepsilon}$, respectively. In this work, we follow the framework described by Papalexandris in [18] to immiscible mixtures whose constituents are in thermal non-equilibrium. We can then define ρ, $\boldsymbol{u} = (u, v)$, p, e_t that respectively denote the density, velocity vector, pressure and total energy of the fluid. All variables relative to the fluid phase only, are defined in the entire domain. In view of the constitutive assumptions (1)-(4), and after some algebraic operations, the mass, momentum and energy balance laws for the fluid phase are :

$$\frac{\mathrm{d}(\phi\rho)}{\mathrm{d}t} + \phi\rho\nabla\cdot\boldsymbol{u} = \mathcal{M} \tag{A.1}$$

$$\phi\rho\frac{\mathrm{d}\boldsymbol{u}}{\mathrm{d}t} + \nabla(\phi p) = \nabla\cdot(\phi\boldsymbol{P}_d^v) - \nabla(\phi p^v) + \boldsymbol{f} - \mathcal{M}\boldsymbol{u} + \phi\rho\boldsymbol{g} \tag{A.2}$$

$$\phi\rho\frac{\mathrm{d}e}{\mathrm{d}t} + \phi p\nabla\cdot\boldsymbol{u} = \phi\boldsymbol{P}_d^v : \boldsymbol{V}_d^v - \phi p^v\nabla\cdot\boldsymbol{u} - \nabla\cdot(\phi\boldsymbol{q}) + \boldsymbol{\varepsilon} - \boldsymbol{f}\cdot\boldsymbol{u} - \mathcal{M}(e - \frac{1}{2}\boldsymbol{u}\boldsymbol{u}) \tag{A.3}$$

where V_d^v stands for the deviatoric part of the deformation tensor, $\mathrm{d}/\mathrm{dt}()$ stands for the material derivative with respect to the fluid velocity, and where the total energy e_t is the sum of the fluid's internal and kinetic energies

$$e_t = e + \frac{1}{2}\boldsymbol{u}\cdot\boldsymbol{u} \tag{A.4}$$

In the above equations, q is the conductive heat flux for the fluid phase, g is the vector of gravitational acceleration and $\boldsymbol{P}^v$ Pv is for the viscous stress tensor

of the fluid. By virtue of the isotropy of the fluid and the conservation of angular momentum, this tensor is symmetric. It is then decomposed according to

$$\boldsymbol{P}^v = -p^v \boldsymbol{I} + \boldsymbol{P}_d^v \qquad p^v = -\frac{1}{3} tr\left(\boldsymbol{P}^v\right) \tag{A.5}$$

where p^v is the bulk viscous pressure and $\boldsymbol{P}_d^v$ is the (deviatoric) viscous shear stress tensor.

Similarly, let ρ_s, p_s, e_s denote the density, pressure (trace of the stress tensor) and internal energy of the solid matrix, respectively. These variables, and all variables to the solid matrix only, are defined in the porous region Ω_p. By virtue of the assumptions (1)-(5), and knowing that the density of the solid phase is constant, the balance laws for the solid matrix read:

$$\frac{\partial \phi}{\partial t} = \frac{1}{\rho_s} \mathcal{M} \tag{A.6}$$

$$\nabla((1-\phi)p_s) + \nabla \cdot ((1-\phi)\boldsymbol{\tau}_s) = -\boldsymbol{f} + (1-\phi)\rho_s \boldsymbol{g} \tag{A.7}$$

$$(1-\phi)\rho_s \frac{\partial e_s}{\partial t} = -\nabla \cdot ((1-\phi)\boldsymbol{q}_s) - \varepsilon + \mathcal{M} e_s \tag{A.8}$$

where τ_s and $\boldsymbol{q}_s$ stands for the deviatoric part of the stress tensor and the conductive heat flux of the solid matrix, respectively.

The next step is to derive a balance law for the mixture's entropy. To this end, we first introduce the mixture's density ρ_m, barycentric velocity u_m and specific entropy S_m, respectively :

$$\rho_\mathrm{m} = \phi\rho + (1-\phi)\rho_s \qquad \boldsymbol{u}_\mathrm{m} = \frac{\phi\rho\boldsymbol{u}}{\rho_\mathrm{m}} \qquad S_\mathrm{m} = \frac{\phi\rho S + (1-\phi)\rho_s S_s}{\rho_\mathrm{m}} \tag{A.9}$$

Also, let $\mathrm{d}/\mathrm{d}_\mathrm{m}()$ stand for the material derivative with respect to the mixture's barycentric velocity, $d/dmt() = (\partial/\partial t + \boldsymbol{u}_\mathrm{m} \cdot \nabla)\,()$. Using the Gibbs relations of the 2 phases and their balance equations, we obtain the balance law for the mixture's entropy in the form

$$\rho_m \frac{\mathrm{d}S_m}{\mathrm{d}_m t} = \nabla \cdot \boldsymbol{J} + \sigma \tag{A.10}$$

where $\boldsymbol{J}$ is the mixture's entropy flux. As such, $\nabla \cdot \boldsymbol{J}$ can be either positive or negative. The term σ represents the entropy production rate and has to be non-negative in accordance with the entropy axiom $\sigma \geq 0$.

For the mixture in hand, by inputing the Gibbs relations of the 2 phases in their respective balance equations, we have that

$$\boldsymbol{J} = \frac{1}{T}\boldsymbol{q} + \frac{1}{T_s}\boldsymbol{q}_s + \phi\rho S(\boldsymbol{u}_\mathrm{m} - \boldsymbol{u}) + (1-\phi)\rho_s S_s \boldsymbol{u}_\mathrm{m} \tag{A.11}$$

and that

$$\begin{aligned}\sigma =& \frac{\phi}{T}\boldsymbol{P}_d^v : \boldsymbol{V}_d^v - \frac{\phi}{T}p^v \nabla \cdot \boldsymbol{u} + \phi \boldsymbol{q} \cdot \nabla(T^{-1}) + (1-\phi) + (1-\phi)\boldsymbol{q}_s \cdot \nabla(T_s^{-1}) \\ &+ \mathcal{M}\mathcal{A} - (\boldsymbol{f} - p\nabla\phi) \cdot \frac{1}{T}\boldsymbol{u} + \boldsymbol{\varepsilon}\left(\frac{1}{T} - \frac{1}{T_s}\right)\end{aligned} \tag{A.12}$$

where $\mathcal{A}$ is the affinity of the interphasial mass exchange and is given by

$$\mathcal{A} = \left(\frac{\psi_s}{T_s} - \frac{\psi}{T} + \frac{p}{T}\left(\frac{1}{\rho_s} - \frac{1}{\rho}\right) + \frac{1}{2T}\boldsymbol{u} \cdot \boldsymbol{u}\right) \tag{A.13}$$

with $\psi = e - ST$ and $\psi_s = e_s - S_s T_s$ being the Helmholtz free energies of fluid and solid phase respectively.
The entropy production rate σ is given as a sum of products. The first terms are of these products are identified as the "thermodynamic current" J_i and the second ones as the "thermodynamics forces" X_i [10]. We then have

$$\sigma = \sum_i J_i X_i \geq 0 \tag{A.14}$$

In order to close the system governing equations (A.1)-(A.3) and (A.6)-(A.8), constitutive relations must be provided between the above currents and forces. The simplest choice is to assume linear relations between them, doing so we have

$$J_i = \sum_i L_{ij} X_j \tag{A.15}$$

where the quantities L_{ij} are the phenomenological coefficients of the mathematical model and are functions of the thermo-mechanical variables of the mixture. The

values of the phenomenological coefficients are constrained by the requirement that the entropy production rate, σ, be non-negative. To further constrains the values of theses coefficients, we invoke the Onsager-Casimir reciprocal relations. Herein, we make the commonly used assumption that the couplings between non-conjugate currents and forces are altogether negligible. This is equivalent to assuming that the matrix of phenomenological coefficients is diagonal ($L_{ij} = 0$ for $i \neq j$). We arrive at the following linear constitutive relations for the viscous stresses and for the conductive heat fluxes:

$$\boldsymbol{P}_d^v = L_{11}\frac{\phi}{T}\boldsymbol{V}_m^v \qquad p^v = -L_{22}\frac{\phi}{T}\nabla\cdot\boldsymbol{u} \qquad \boldsymbol{q} = L_{33}\phi\nabla(T^{-1}) \qquad \boldsymbol{q}_s = \underset{\sim}{\boldsymbol{L}}_{44}(1-\phi)\nabla(T_s^{-1}) \tag{A.16}$$

and the interphasial relaxation phenomena

$$\mathcal{M} = L_{55}\mathcal{A} \qquad \boldsymbol{f} - p\nabla\phi = -\underset{\sim}{\boldsymbol{L}}_{66}\frac{1}{T}\boldsymbol{u} \qquad \boldsymbol{\varepsilon} = L_{77}(\frac{1}{T_s} - \frac{1}{T}) \tag{A.17}$$

In these equations all phenomenological coefficients are scalar, except for $\underset{\sim}{\boldsymbol{L}}_{44}$ and $\underset{\sim}{\boldsymbol{L}}_{66}$ which, in the general case, are 2^{nd} order tensors due to the anisotropy of the solid matrix. The first four phenomoligical coefficients are related to the fluid shear and bulk viscosities μ and ζ, and fluid and solid conductivities k and $\underset{\sim}{\boldsymbol{k}}_s$ and the 3 others are related to the via the following equations interphasial mass and heat transfer coefficients and drag-parameter tensor

$$L_{11} = \frac{T}{2\phi}\mu \quad L_{22} = \frac{T}{\phi}\zeta \quad L_{33} = \frac{T^2}{\phi}k \quad \underset{\sim}{\boldsymbol{L}}_{44} = \frac{T_s^2}{1-\phi}\underset{\sim}{\boldsymbol{k}}_s \quad \kappa = L_{55} \quad h = -\frac{L_{77}}{TT_s} \quad \underset{\sim}{\boldsymbol{\beta}} = \frac{\underset{\sim}{\boldsymbol{L}}_{66}}{T} \tag{A.18}$$

so that the equations (A.16) can be rewritten using Newton's law of viscosity and Fourier law of heat conduction

$$\boldsymbol{P}_d^v = \mu\boldsymbol{V}_d^v \qquad p^v = -\zeta\nabla\cdot\boldsymbol{u} \qquad \boldsymbol{q} = -k\nabla T \qquad \boldsymbol{q}_s = -\underset{\sim}{\boldsymbol{k}}_s\nabla T_s \tag{A.19}$$

We can also rewrite (A.17) as

$$\mathcal{M} = \kappa\mathcal{A} \qquad \boldsymbol{f} = p\nabla\phi - \underset{\sim}{\boldsymbol{\beta}}\boldsymbol{u} \qquad \boldsymbol{\varepsilon} = h(T_s - T) \tag{A.20}$$

The balance laws (A.1)-(A.8) along with the constitutive relations (A.19)-(A.20) and a state equation for the fluid, constitute a closed system of governing equations for the flows of interest.

All thermodynamic and kinematic variables that appear in the model derived above are well defined in their respective domains of definition. Consequently, the model is formally valid at any length-scale. However, its validity is limited by the continuum hypothesis regarding the porosity distribution, which breaks down at the scale of the porous microstructure. For this reason, in reality it cannot resolve flow scales inside the porous medium whose size is comparable to the length-scale of the porous micro-structure.

Bibliography

[1] R. R. Linn A. Kochanski. "Fire behavior and smoke modeling: Model improvement and measurement needs for next-generation smoke research and forecasting systems". In: *International Journal of Wildland Fire* (2019).

[2] L.M. Ribeiro A.M.G. Lopes. "Simulation of forest fire spread using a two-way coupling algorithm and its application to a real wildfire". In: *Ecological Modelling* 348 (2017), pp. 33–43.

[3] Panagiotis Dimitrios Antoniadis. "Modeling and numerical simulation of transient flows in superposed porous and pure-fluid layers". PhD thesis. 2015.

[4] M.V. Papalexandris C. Varsakelis. "Low-Mach-number asymptotics for two-phase flows of granular materials". In: *J. Fluid Mech.* (2011).

[5] M.V. Papalexandris C. Varsakelis. "The equilibrium limit of a constitutive model for two-phase granular mixtures and its numerical approximation". In: *Journal of Computational Physics* 229 (2010).

[6] Giorgio Crasto. "A canopy model for WindSim 4.5". In: *Forest Modeling*. 2006.

[7] I. Pop D. B. Ingham. "Transport phenomena in porous media". In: vol. 3. Elsevier, 2005, pp. 287–305.

[8] F.A.L Dullien. *Porous media: Fluid transport and pore structure*. Academic Press, 1992.

[9] J.M. Przybylski E. Noordally J.J. Witton. *Porous media combustors for clean gas turbine engines*. Tech. rep. Cranfield University (United Kingdom), 2004.

[10] D. Jou G. Lebon. *Understanding Non-equilibrium Thermodynamics*. Springer, 2008.

[11] C.K. McMahon H.B. Clements. "Nitrogen oxides from burning forest fuels examined by thermogravimetry and evolved gas analysis". In: *Thermochimica* 35 (1980), pp. 133–139.

[12] Y. Miyairi K. Hanamura K. Bohda. “A study of super-adiabatic combustion engine”. In: *Energy Conversion and Management* 38.10–13 (1997), pp. 1259–1266.

[13] M.R. En Wee K. Mutthulakshmi. “Simulating forest fire spread and fire-fighting using cellular automata”. In: *Chinese Journal of Physics* 65 (2020), pp. 642–650.

[14] A. Mohammadi M. Ziabasharhagh. “Numerical Simulation: From Theory to Industry”. In: ed. by Mykhaylo Andriychuk. InTechOpen, 2012. Chap. 22, pp. 529–556.

[15] M. Shams M. Farzaneh M.S. Dehaj R. Ebrahimi. “Experimental analysis of natural gas combustion in a porous burner”. In: *Experimental Thermal and Fluid Science* 84 (2017), pp. 134–143.

[16] E. A. Johnson K. Miyanishi. *Forest Fires : Behavior and Ecological Effects*. Academic Press, 2001.

[17] G. C. Krieger P. Bufacchi. “Numericalsimulationofsurfaceforest fireinBrazilianAmazon”. In: *FireSafetyJournal* 79 (2016), pp. 44–56.

[18] M.V. Papalexandris. “A two-phase model for compressible granular flows based on the theory of irreversible processes”. In: *Journal of Fluid Mechanics* 517 (2004).

[19] M.V. Papalexandris. *Combustion and Fuels*. Lecture notes.

[20] Y. Rogaume. “La combustion du bois et de la biomasse”. In: *Pollution Atmosphérique* (2019).

[21] N.R. Amundson S. Sundaresan. “Diffusion and reaction in a stagnant boundary layer about a carbon particle”. In: *Chem. Fundam.* 19 (1980), pp. 103–112.

[22] S. P. Urbanski. “Combustion efficiency and emission factors for wildfire-season fires in mixed conifer forests of the northern Rocky Mountains, US”. In: *Atmospheric Chemistry and Physics* (2005).

[23] Francis Westley. *Table of Recommended Rate Constants for Chemical Reactions Occuring in Combustion*. National Bureau of Standards. U.S. Department of Commerce, 1980.

[24] W. Huang Z. Zheng. “Forest fire spread simulating model using cellular automaton withextreme learning machine”. In: *Ecological Modelling* 348 (2017), pp. 33–43.

UNIVERSITÉ CATHOLIQUE DE LOUVAIN
École polytechnique de Louvain
Rue Archimède, 1 bte L6.11.01, 1348 Louvain-la-Neuve, Belgique | **www.uclouvain.be/epl**